1 Evaluating the impact of new observational constraints on P-
2 S/IVOC emissions, multi-generation oxidation, and chamber
3 wall losses on SOA modeling for Los Angeles, CA

5 Prettiny K. Ma,[1] Yunliang Zhao,[2] Allen L. Robinson,[2] David R. Worton,[3,a] Allen H.
6 Goldstein,[3,4] Amber M. Ortega,[5,b] Jose L. Jimenez,[5] Peter Zotter,[6,c] André S. H. Prévôt,[6]
7 Sönke Szidat,[7] and Patrick L. Hayes[1]

9 [1]Department of Chemistry, Université de Montréal, Montréal, QC, Canada

10 [2]Center for Atmospheric Particle Studies, Carnegie Mellon University, Pittsburgh, PA,
11 USA

12 [3]Department of Civil and Environmental Engineering, University of California, Berkeley,
13 CA, USA

14 [4]Department of Environmental Science, Policy and Management, University of
15 California, Berkeley, CA, USA

16 [5]Cooperative Institute for Research in the Environmental Sciences and Dept. of
17 Chemistry and Biochemistry, University of Colorado, Boulder, CO, USA

18 [6]Laboratory of Atmospheric Chemistry, Paul Scherrer Institute, Villigen, Switzerland

19 [7]Department of Chemistry and Biochemistry & Oeschger Centre for Climate Change,
20 University of Bern, Bern, Switzerland

21 [a]now at: Gas and Particle Metrology, National Physical Laboratory, Hampton Rd,
22 Teddington, Middlesex, UK

23 [b]now at: Air Pollution Control Division, Colorado Department of Public Health and
24 Environment, Denver, CO, USA

25 [c]now at: Lucerne University of Applied Sciences and Arts, School of Engineering and
26 Architecture, Bioenergy Research, Technikumstrasse 21, CH-6048 Horw, Switzerland

27 *Correspondence to:* Patrick L. Hayes (patrick.hayes@umontreal.ca)

29   **ABSTRACT**

30   Secondary Organic Aerosols (SOA) are important contributors to fine PM mass in
31   polluted regions, and their modeling remains poorly constrained. A box model is
32   developed that uses recently published literature parameterizations and data sets to better
33   constrain and evaluate the formation pathways and precursors of urban SOA during the
34   CalNex 2010 campaign in Los Angeles. When using the measurements of IVOCs
35   reported in Zhao et al. (2014) and of SVOCs reported in Worton et al. (2014) the model
36   is biased high at longer photochemical ages whereas at shorter photochemical ages it is
37   biased low, if the yields for VOC oxidation are not updated. The parameterizations using
38   an updated version of the yields, which takes into account the effect of gas phase wall-
39   losses in environmental chambers, show model/measurement agreement at longer
40   photochemical ages, even though some low bias at short photochemical ages still
41   remains. Furthermore, the fossil/non-fossil carbon split of urban SOA simulated by the
42   model is consistent with measurements at the Pasadena ground site.

43   Multi-generation oxidation mechanisms are often employed in SOA models to
44   increase the SOA yields derived from environmental chamber experiments in order to
45   obtain better model/measurement agreement. However, there are many uncertainties
46   associated with these ''aging'' mechanisms. Thus, SOA formation in the model is
47   compared against data from an oxidation flow reactor (OFR) in order to constrain SOA
48   formation at longer photochemical ages than observed in urban air. The model predicts
49   similar SOA mass when the ''aging'' mechanisms or the updated version of the yields for
50   VOC oxidation are implemented. The latter case though has SOA formation rates that are
51   more consistent with observations from the OFR.

52   All the model cases evaluated in this work have a large majority of the urban SOA
53   (70 − 86 %) at Pasadena coming from the oxidation of P-SVOCs and P-IVOCs. The
54   importance of these two types of precursors is further supported by analyzing the
55   percentage of SOA formed at long photochemical ages (1.5 days) as a function of the
56   precursor rate constant. The P-SVOCs and P-IVOCs have rate constants that are similar
57   to highly reactive VOCs that have been previously found to strongly correlate with SOA
58   formation potential measured by the OFR.

59   Finally, the volatility distribution of the total organic mass (gas and particle
60   phase) in the model is compared against measurements. The total SVOC mass simulated
61   is similar to the measurements, but there are important differences in the measured and
62   modeled volatility distributions. A likely reason for the difference is the lack of particle-
63   phase reactions in the model that can oligomerize and/or continue to oxidize organic
64   compounds even after they partition to the particle phase.

65

1. INTRODUCTION

66

67   Atmospheric aerosols are important climate forcing agents (Christensen et al.,
68   2013), negatively impact human health (Dockery and Pope, 1994) and reduce visibility
69   by scattering and absorbing light (Watson, 2002). However, predicting quantitatively the
70   composition and concentrations of aerosols is challenging, in part because of their
71   complex composition and the variety of emission sources and chemical pathways that
72   contribute to aerosol loadings in the atmosphere (Heald et al., 2011; Spracklen et al.,
73   2011). Atmospheric aerosols are composed of black carbon, inorganic, and organic
74   matter, and the latter is a mixture of hundreds to thousands of compounds (Gentner et al.,
75   2012).

76   Due to this complexity, organic aerosol is often categorized into two groups.
77   Primary organic aerosol (POA) is directly emitted into the atmosphere from sources such
78   as motor vehicles, food cooking, and biomass burning (Hallquist et al., 2009). On the
79   other hand, secondary organic aerosol (SOA) is the product of diverse chemical reactions
80   occurring in the atmosphere that transform more-volatile precursors such as volatile
81   organic compounds (VOCs) into lower volatility products that are either incorporated
82   into existing particles or nucleate new particles. Many previous studies have shown that
83   SOA is an important fraction of OA globally often representing more than half the total
84   OA concentration (Jimenez et al., 2009; Zhang et al., 2007).

85   In SOA parameterizations for use in regional and global models, a semi-empirical
86   approach is used in which VOCs, often the only SOA precursors considered, react with
87   OH radicals and other oxidants to form secondary products with lower volatility at a
88   given mass yield. These secondary semi-volatile organic compounds (SVOCs) can
89   partition to the particle phase to form SOA (Donahue et al., 2006; Odum et al., 1996;
90   Pankow, 1994). The parameters used in the models for the VOCs, such as the yields and
91   product volatilities, are often determined from published chambers studies (e.g. Presto et
92   al., 2010; Chan et al., 2009; Hallquist et al., 2009; Kroll et al., 2006). Over the past
93   decade a number of studies have shown that traditional models that consider only the
94   oxidation of VOCs alone predict SOA concentrations much lower than those observed in
95   polluted urban regions (Hayes et al., 2015; Hodzic and Jimenez, 2011; Dzepina et al.,
96   2009; Volkamer et al., 2006). As a result, several updates have been proposed in the
97   literature to improve SOA models including new pathways for SOA formation, new SOA
98   precursors, and increased yields for known precursors (e.g. Ervens and Volkamer, 2010;
99   Ng et al., 2007; Robinson et al., 2007).

100   The volatility basis-set (VBS) approach (Donahue et al., 2006) has been used in
101   most recent parameterizations of SOA yields. In this approach, the organic mass is
102   distributed in logarithmically spaced volatility bins, and the SOA forming reactions then
103   redistribute the mass from precursors such as anthropogenic and biogenic VOCs, into

104 bins with generally lower volatility (except for fragmentation reactions) leading to
105 increased OA concentrations (Tsimpidi et al., 2010; Robinson et al., 2007). While the
106 VBS provides a valuable conceptual framework for SOA modeling, substantial
107 uncertainties remain in the correct parameters for different precursors and conditions.

108   In this paper we focus on investigating three interrelated questions that are
109 responsible for important uncertainties in urban SOA modeling. The first is how to best
110 incorporate SOA from primary semi- and intermediate volatility compounds (P-
111 S/IVOCs), two recently-proposed types of SOA precursors. While there is now ample
112 evidence that P-S/IVOCs are important contributors to SOA (Zhao et al., 2014; Robinson
113 et al., 2007), the emissions of these precursors as well as the parameters that govern their
114 oxidation and SOA formation are not well constrained. Also, it is well known that models
115 of SOA that incorporate P-S/IVOCs often do not agree with measurements across a range
116 of photochemical ages, although the modeled SOA mass varies substantially with the
117 parameterization used. (Fountoukis et al., 2016; Woody et al., 2016; Hayes et al., 2015;
118 Dzepina et al., 2009). The second question is whether loses of semi-volatile gases to the
119 walls of environmental chambers (Krechmer et al., 2016; Matsunaga and Ziemann, 2010)
120 have resulted in low biases for the yields of some or all precursors, especially VOCs, as
121 has been recently reported (Zhang et al., 2014). The third question is the appropriateness
122 of including "aging" mechanisms in the VBS parameterization of SOA from VOCs, in
123 which the initial oxidation reaction is followed by subsequent oxidation reactions of the
124 first and later generation products, with each reaction resulting in a reduction of the
125 organic volatility by, e.g., an order of magnitude. These "aging" mechanisms increase
126 VOC yields to levels much higher than those observed in chamber studies. In some
127 model applications they improve model agreement with field measurements (Ahmadov et
128 al., 2012), while in other cases they lead to model SOA formation that is substantially
129 larger than observed (e.g. Hayes et al., 2015; Dzepina et al., 2011; 2009) While the
130 inclusion of some of these new SOA precursors, updated yields, and aging can provide in
131 some cases better agreement with measurements, the relative amount of SOA formed
132 from VOCs (V-SOA), P-IVOCs (I-SOA), and P-SVOCs (S-SOA) is highly uncertain,
133 and changes strongly depending on which of the above updates are implemented in a
134 specific model. In addition, the fact that different subsets and variants of these updates
135 can allow specific models to match SOA measurements raises important questions
136 regarding whether or not the model mechanisms are representative of actual SOA
137 forming processes in the atmosphere.

138   Recently, we evaluated three parameterizations for the formation of S-SOA and I-
139 SOA using a constrained 0-D box model that represents the South Coast Air Basin during
140 the California Research at the Nexus of Air Quality and Climate Change (CalNex)
141 campaign (Hayes et al., 2015). The box model allowed the evaluation of multiple model
142 parameterizations previously proposed in the literature and the performance of sensitivity

143 studies, which would be difficult to carry-out in more computationally demanding
144 gridded 3-D models. The results obtained indicated that different combinations of
145 parameterizations could reproduce the total SOA equally well even though the amounts
146 of V-SOA, I-SOA, and S-SOA were very different. In addition, the model over-predicted
147 SOA formed at longer photochemical ages ($\approx$ 3 days) when compared to observations
148 downwind of multiple urban sites. This discrepancy suggests that the ratio of P-S/IVOCs-
149 to-POA may have been too high in the parameterizations evaluated. Also, as mentioned
150 previously and discussed in Hayes et al. (2015), the implementation of aging for VOC
151 products remains uncertain.

152 The goal of this study is to use several recently published results to better evaluate
153 and constrain the box model introduced in our previous work, and thus facilitate the
154 identification of parameterizations that can be eventually incorporated into 3-D air
155 quality models to accurately predict SOA for the right reasons. In particular, our work
156 here improves the box model by incorporating recently published measurements of P-
157 IVOCs and P-SVOCs that allow better constraining of the concentration, reactivity,
158 yields, and volatility of these precursors (Worton et al., 2014; Zhao et al., 2014). In
159 addition, given that experiments in environmental chambers may underestimate SOA
160 yields for the VOCs due to losses of semi-volatile gases to the chamber walls (Zhang et
161 al., 2014), the SOA yields from VOCs have been re-estimated using a very recent
162 parameterization of these wall-losses (Krechmer et al., 2016). The wall-loss corrected
163 yields obtained are then used in the model in a sensitivity study to evaluate the
164 corresponding change in the modeled SOA concentrations. The results obtained from the
165 new box model are also compared against ambient ground site and airborne
166 measurements, and also against recently-published oxidation flow reactor (OFR)
167 measurements (Ortega et al., 2016). This combination of data sets allows the model to be
168 evaluated for photochemical ages ranging up to 3 equivalent days (at 1.5×10^6 molec OH
169 cm^{-3}) providing a means to evaluate the aging mechanisms of the VOCs in the VBS.

2. EXPERIMENTAL SECTION

2.1 Measurement and sampling site

172 The box model is constructed in order to represent the South Coast Air Basin
173 during CalNex in spring/summer 2010. The measurements of aerosols used in this study
174 were conducted in Pasadena, California (34.1406° N 118.1224° W), located to the
175 northeast of downtown Los Angeles (Hayes et al., 2015). An overview of CalNex has
176 been published previously (Ryerson et al., 2013). The location and the meteorology of the
177 ground site at Pasadena are described in further detail in Hayes et al. (2013). Pasadena is
178 a receptor site for pollution due to winds that transport emissions from the Ports of Los
179 Angeles and Long Beach and downtown Los Angeles. Airborne measurements of

180   aerosols were also carried out in the South Coast Air Basin as part of the CalNex project.
181   A detailed description of the airborne measurements is given in Bahreini et al. (2012).
182   Furthermore, measurements of POA composition and volatility taken at the Caldecott
183   Tunnel in the San Francisco Bay Area reported in previous work (Worton et al., 2014)
184   are also used to constrain the model as described below. The tunnel air samples were
185   collected during July 2010. It should be noted that the tunnel measurements do not
186   include emissions due to cold starts of vehicles. In the box model, only the relative
187   volatility distribution of vehicular POA measured during the tunnel study is used, and
188   thus this potential source of error does not apply to the total amount of vehicular POA
189   emissions in the model.

190   Two additional datasets are used to evaluate the model. In addition to sampling
191   ambient air, an aerosol mass spectrometer (AMS) sampled air that had been
192   photochemically aged using an oxidation flow reactor (OFR) (Ortega et al., 2016). The
193   OFR exposed ambient air to varying concentrations OH radicals in order to obtain
194   photochemical ages much higher than the ambient levels observed at the Pasadena site,
195   and the amount of SOA produced was quantified as a function of OH exposure.
196   Moreover, radiocarbon (^{14}C) analysis has been performed on filter samples and results
197   were combined with positive matrix factorization (PMF) data to determine fossil and
198   non-fossil fractions of the SOA components as reported in Zotter et al. (2014). The ^{14}C
199   results are used for subsequent comparison against the box model from which fossil and
200   non-fossil SOA mass can be estimated.

201   **2.2 Model set-up**

202   The SOA model is set-up to include 3 types of precursors: VOCs, P-IVOCs, and
203   P-SVOCs. The parameters used in the box model to simulate the formation of SOA from
204   these precursors are listed in Tables S1 to S3 of the supporting information. The box
205   model dynamically calculates the evolution of organic species in an air parcel as it
206   undergoes photochemical aging, hence producing SOA. The total SOA also includes
207   background SOA (BG-SOA) at a constant concentration of 2.1 µg m^{-3}, as determined in
208   our previous work (Hayes et al., 2015). The model accounts for P-SVOC emissions from
209   vehicular exhaust and cooking and treats POA as semi-volatile (Robinson et al., 2007).

210   A schematic of the model is shown in Figure 1. All the model cases are listed in
211   Table 1, and all the parameterizations are shown schematically in Figure 2. The first
212   model case (ROB + TSI) incorporates the Robinson et al. (2007) parameterization for
213   SOA formation that models P-IVOCs and P-SVOCs (i.e. P-S/IVOCs) using a single
214   volatility distribution and oxidation rate constant. The ROB + TSI case also uses the
215   Tsimpidi et al. (2010) parameterization for SOA formation from VOCs. A detailed
216   description of the parameters used in ROB + TSI can be found in Hayes et al. (2015), and
217   the ROB + TSI model case used here is identical to the case of the same name used in

218   that paper. Briefly, as displayed in Fig. 2A, the Tsimpidi et al. (2010) parameterization
219   proposes that the VOCs undergo an initial oxidation step that will form four lumped
220   products with different volatilities ($c^* = 1, 10^1, 10^2, 10^3$ µg m^{-3}, where c^* is the effective
221   saturation concentration). The first-generation oxidation products can be further oxidized,
222   decreasing their volatility by one order of magnitude (i.e. aging). This "bin-hopping"
223   mechanism repeats until the lowest volatility product is reached ($c^* = 10^{-1}$ µg m^{-3} in this
224   study and 1 µg m^{-3} in other studies such as Tsimpidi et al. (2010) and Hayes et al. (2015).
225   The Robinson et al. (2007) parameterization proposes that the P-S/IVOCs are initially
226   distributed in logarithmically spaced volatility bins ranging from $c^* = 10^{-2}$ to 10^6 µg m^{-3}.
227   Thereafter, the oxidation of P-S/IVOCs decreases their volatility by one order of
228   magnitude until the lowest volatility product is reached ($c^* = 10^{-2}$ µg m^{-3}). The lowest
229   volatility product possible is not the same for the oxidation of VOCs versus the oxidation
230   of the P-S/IVOCs (10^{-1} vs. 10^{-2} µg m^{-3}, respectively). However, whether the mass is
231   distributed into either bin has a negligible effect on the SOA mass simulated in the box
232   model because of the relatively high SOA concentrations during the case study.

233   In this work, 5 model parameterizations are tested that incorporate new
234   measurements of IVOCs and P-SVOC volatility as well as updated VOC yields that
235   account for wall-losses of vapors (Krechmer et al., 2016; Zhang et al., 2014). For the first
236   new case (ROB + ZHAO + TSI), we incorporate IVOC data measured in Pasadena
237   during the CalNex campaign as reported from Zhao et al. (2014). In particular, the
238   measured concentrations of speciated and unspeciated IVOCs and their estimated
239   volatility are used to constrain the initial concentration of these species (as discussed in
240   Section 2.2.2 below) as well as to estimate their yields (Zhao et al., 2014). Therefore, we
241   replace the inferred concentrations of IVOCs that were used in our previous work and
242   based on the volatility distribution of Robinson et al. (2007) with concentrations that are
243   directly constrained by measurements. In the ROB + ZHAO + TSI case the SOA
244   formation parameters used (e.g. yields, oxidation rate constants) are taken from Zhao et
245   al. (2014) for the IVOCs and from Hayes et al. (2015) for the VOCs and SVOCs.

246   For the second new case (WOR + ZHAO + TSI), the volatility distribution of P-
247   SVOCs is updated using measurements of POA performed at the Caldecott tunnel in the
248   California Bay Area (Worton et al., 2014). In the previous two cases described above, the
249   relative volatility distribution of P-SVOCs was taken from the work of Robinson et al.
250   (2007). In this distribution, the relative concentration of SVOCs increases monotonically
251   between the c^* bins 10^{-2} and 10^2 µg m^{-3}. The P-SVOC volatility distribution in the WOR
252   + ZHAO + TSI case increases monotonically as well, but the relative concentrations in
253   each bin are different and notably there is a much higher relative concentration of SVOCs
254   in the $c^* = 10^2$ µg m^{-3} bin (see Fig. 2 and Table S3 in the supporting information). In this
255   model case, the updated P-SVOC volatility distribution is only applied to vehicular P-
256   S/IVOCs. The volatility distribution proposed by Robinson et al. (2007) is still used for

cooking emissions since no distribution specific to these emissions is available in the
literature to our knowledge.

Several recently published papers have found that chamber experiments may
underestimate SOA yields due to the loss of semi-volatile vapors to chamber walls
(Krechmer et al., 2016; Zhang et al., 2014; Matsunaga and Ziemann, 2010). A sensitivity
study has been performed to explore this uncertainty by running the three model cases
described above (ROB + TSI, ROB + ZHAO + TSI, and WOR + ZHAO + TSI) with a
revised version of the SOA yields for VOCs that accounts for these wall losses. A
detailed description of how these updated yields were estimated is provided in the
supporting information and the values can be found in Table S4. Briefly, equilibrium
partitioning is assumed to hold for the organic mass found in the gas phase, particle
phase, or chamber walls. The SOA yields are then obtained by refitting SOA chamber
yield curves using a model that accounts for partitioning between the three compartments
(particle, gas, and wall) and incorporates the equivalent wall mass concentrations
published in Krechmer et al. (2016), which are volatility dependent. The SOA chamber
yield curves that were refitted were first calculated using the parameters published in
Tsimpidi et al. (2010). There are limits to the assumption that partitioning between the
three phases occurs on short enough timescales for all four VOC product volatilities that
equilibrium is reached during an SOA chamber study. Specifically, at lower volatilities
($c^* \approx 1$ μg m^{-3}), the partitioning kinetics of the organic mass from the particles to the
chamber walls have a timescale that is longer than typical chamber experiments (Ye et
al., 2016). As described in the supporting information, the updated SOA yields for VOC
oxidation should therefore be considered upper limits, whereas the original yields serve
as lower limits.

According to Krechmer et al. (2016) and other chamber experiments (Matsunaga
and Ziemann, 2010), the gas-wall equilibrium timescale doesn't vary strongly with the
chamber size. Similar timescales have been calculated for a variety of environmental
chambers, including chambers that were used to determine many of the yields used in this
paper. In addition, Matsunaga and Ziemann found that partitioning was nearly
independent of chamber treatment, reversible, and obeyed Henry's law. Thus, the
effective wall concentrations determined from the chamber experiments reported in
Krechmer et al. (2016) are likely applicable to other chambers with different sizes.

The three model cases accounting for wall losses of organic vapors are named
ROB + MA, ROB + ZHAO + MA, and WOR + ZHAO + MA. For these cases, the aging
of the secondary SVOCs formed from the oxidation of VOCs was not included, since
multi-generation oxidation is not well-constrained using data from chamber studies that
are run over relatively short time-scales (i.e. hours). In addition, aging and correcting for
wall-losses of organic vapors have been separately proposed to close the gap between
observed and predicted SOA concentration from pre-2007 models. The aging of

296 secondary SVOCs formed from the oxidation of P-IVOCs (and P-SVOCs) has been kept
297 for all of the MA cases, however. A similar approach for correcting the yields as
298 described above cannot be applied to P-IVOCs because organics with low volatilities (c^*
299 < 10 μg m^{-3}) will partition to chamber walls very slowly, and SVOCs from P-IVOC
300 oxidation tend to have lower volatilities than the SVOCs formed from VOC oxidation
301 (Tables S1 and S2). Indeed, when trying to refit the IVOC yield curves, the model
302 assuming equilibrium partitioning between particles, the gas phase, and the walls was not
303 able to reproduce the chamber data, which would be consistent with equilibrium not
304 having been reached during the chamber studies.

2.2.1 IVOC oxidation parameterizations

306 An important difference between the ROB + TSI and ROB + MA cases and the
307 other four cases that have been updated with the IVOC measurements of Zhao et al.
308 (2014) is that in the ZHAO cases, the first generation of IVOC oxidation distributes part
309 of the product mass into four different volatility bins ($C^* = 10^{-1}$, 1, 10^1, 10^2 μg m^{-3}) as is
310 displayed in Fig. 2E. This IVOC oxidation scheme is similar to that used for the first step
311 of VOC oxidation (Tsimpidi et al., 2010) as displayed in Fig. 2A and D, and has been
312 used to model chamber measurements of SOA from IVOCs (Presto et al., 2010).
313 Contrastingly, in the ROB + TSI and ROB + MA cases, a "bin-hopping" approach is used
314 for all P-S/IVOCs where oxidation lowers volatility by only one order of magnitude (see
315 Fig. 2B and C). The Robinson et al. (2007) parameters are still used for the formation of
316 SOA from P-SVOCs in the ROB + ZHAO + TSI and ROB + ZHAO + MA cases, but the
317 parameters are only applied to primary emissions in c^* bins between 10^{-2} and 10^2 μg m^{-3}
318 inclusive (i.e. the volatilities corresponding to P-SVOCs).

2.2.2. Determination of initial precursor concentrations

320 In the ROB + TSI and ROB + MA cases, the initial concentration of P-S/IVOCs is
321 estimated as follows. The volatility distribution determined by Robinson et al. (2007) is
322 assumed to represent all P-S/IVOCs emitted (Dzepina et al., 2009). The total
323 concentration of P-S/IVOCs is then set so that the amount of P-S/IVOCs in the particle
324 phase is equal to the initial POA concentration. The initial POA concentration is
325 determined from the product of the background-subtracted CO concentration and the
326 ΔPOA/ΔCO emission ratio (Hayes et al., 2015). The same method is used for the other
327 four model cases, but only the initial concentration of P-SVOCs is estimated by this
328 method and the initial concentration of P-IVOCs is estimated separately as described in
329 the next paragraph. In addition, in the WOR + ZHAO + TSI and WOR + ZHAO + MA
330 cases the volatility distribution of vehicular P-SVOCs reported in Worton et al. (2014) is
331 used for estimating the initial concentration of vehicular P-SVOCs whereas the volatility

332 distribution of Robinson et al. (2007) is used for estimating the initial concentration of
333 cooking P-SVOCs.

334   The initial concentrations of VOCs and IVOCs are calculated by multiplying the
335 background-subtracted CO concentrations measured at Pasadena by the emission ratios
336 ΔVOC/ΔCO or ΔIVOC/ΔCO. In the ROB + TSI and ROB + MA cases this method is
337 only applied to the VOCs. The initialization method for the concentrations of the VOCs
338 is the same for all six cases in this paper. For the biogenic VOCs, we follow the same
339 method as Hayes et al. (2015) to determine the initial concentrations since these
340 compounds are not co-emitted with CO (Hayes et al., 2015). The emission ratios are
341 taken from the literature when available (Borbon et al., 2013; Warneke et al., 2007). For
342 most of the IVOCs and some VOCs, emission ratios are not available in the literature.
343 The ratios are instead determined by performing linear regression analyses on scatter
344 plots of the IVOC or VOC and CO concentrations measured in Pasadena between 00:00-
345 06:00 local time when the amount of photochemical aging was very low. The slope of the
346 resulting line corresponds to the estimated emission ratio.

2.3 SOA model

348   The VOC yields are taken from Tsimpidi et al. (2010) or determined in this work
349 as described below. The estimation of the IVOC yields (based on values taken from
350 Presto et al. (2010) and of the OH reaction rate constants for IVOCs follows the same
351 approach used by Zhao et al. (2014). However, instead of using the total SOA yield, Y,
352 for a fixed OA concentration as reported in Zhao et al. (2014), we use the SVOC yield, α,
353 of each c^* bin. It is important to note here that the SOA yields taken from Tsimpidi et al.
354 and Presto et al. use a four-product basis set with $c^* = 10^0, 10^1, 10^2, 10^3$ µg m^{-3} and $c^* =$
355 $10^{-1}, 10^0, 10^1, 10^2$ µg m^{-3} respectively. For this box model, it is more appropriate to have
356 a uniform VBS in terms of the bin range utilised so a bin with a lower volatility ($c^* = 10^{-1}$
357 µg m^{-3}) has been added to the VBS distribution of Tsimpidi et al. (2010). The yield for
358 bin $c^* = 10^{-1}$ µg m^{-3} is 0 for VOC oxidation, but when aging occurs mass can be
359 transferred into this bin. However, the change in the total V-SOA mass is negligible
360 because for both bin $c^* = 10^{-1}$ and 10^0 µg m^{-3} the secondary products almost completely
361 partition to the particle phase.

362   The OH reaction rate constants are taken from the literature (Carter, 2010;
363 Atkinson and Arey, 2003) as described previously in Hayes et al. (2015). During aging,
364 the oxidation products undergo subsequent reactions with OH radicals with a reaction
365 rate constant of 1×10^{-11} cm^3 molec^{-1} s^{-1} and 4×10^{-11} cm^3 molec^{-1} s^{-1} for the products of
366 VOC oxidation and P-S/IVOC oxidation respectively (Hayes et al., 2015). For each
367 oxidation step during aging, there is a mass increase of 7.5 % due to added oxygen.

368   The gas-particle partitioning is calculated in each bin by using the reformulation
369   of Pankow theory by Donahue et al. (2006).

$$x_{p,i} = \left(1 + \frac{C_i}{C_{OA}}\right)^{-1} ; C_{OA} = \sum_i [\text{SVOC}]_i \, x_{p,i}$$

370   Where $x_{p,i}$ is the particle phase fraction of lumped species i; C_i is the effective saturation
371   concentration, and C_{OA} is the total mass of organic aerosol available for partitioning (μg
372   m^{-3}). Only species in the gas phase are allowed to react with OH radicals in the model,
373   since aerosol species react at much lower rates (Donahue et al., 2013).

374   The simulated SOA mass from the model is compared against field measurements
375   of aerosol composition including results from PMF analysis of aerosol mass spectrometry
376   data (Hayes et al., 2015, 2013). Specifically, the model predictions of urban SOA (i.e.
377   SOA formed within the South Coast Air Basin) are compared against the semi-volatile
378   oxygenated organic aerosol (SV-OOA) concentration from the PMF analysis. The other
379   OA component also attributed to SOA, low-volatility oxygenated organic aerosol (LV-
380   OOA), is primarily from precursors emitted outside the South Coast Air Basin and is
381   used to estimate the background secondary organic aerosol (BG-SOA) as discussed
382   previously (Hayes et al., 2015).

383   **3. RESULTS AND DISCUSSION**

384   **3.1 Evolution of SOA concentration over 3 days**

385   We follow an approach similar to Hayes et al. (2015) in order to analyse the
386   model results. The model SOA concentration is normalized to the background subtracted
387   CO concentration to account for dilution, and the ratio is then plotted against
388   photochemical age rather than time to remove variations due to diurnal cycles of
389   precursor and oxidant concentrations. The photochemical age is calculated at a reference
390   OH radical concentration of 1.5×10^6 molec cm^{-3} (DeCarlo et al., 2010). Figure 3 shows
391   this analysis for each model case for up to 3 days of photochemical aging. Since
392   fragmentation and dry deposition are not included in the model, it has only been run to 3
393   days in order to minimize the importance of these processes with respect to SOA
394   concentrations (Ortega et al., 2016).

395   In each panel of Fig. 3, field measurements are included for comparison. The
396   urban SOA mass measured at the Pasadena site is observed at shorter photochemical ages
397   (Hayes et al., 2013). The airborne observations of SOA in the Los Angeles basin outflow
398   is also shown and is the average of all data between 1 and 2 days of photochemical aging
399   (Bahreini et al., 2012). The gray region on the right serves as an estimate for very aged
400   urban SOA based on data reported by de Gouw and Jimenez (2009). The data from the

401   OFR and a fit of the ambient and reactor data (dotted black line) are also displayed in Fig.
402   3 (Ortega et al., 2016). In addition, in Figure 4 the ratio of modeled-to-measured SOA
403   mass is shown on a logarithmic axis to facilitate evaluation of model performance.

404   In ROB + TSI, as described in previous work (Hayes et al., 2015), there is a large
405   over-prediction of SOA mass at longer photochemical ages. As displayed in Fig. 3, the
406   amount of SOA produced in the model is higher than all of the field measurements taken
407   at a photochemical age longer than 0.5 days. Moreover, the ratios of model to
408   measurement are higher than the upper limit of the gray bar representing the ratios within
409   the measurement uncertainties. There is an agreement with the measurements at moderate
410   photochemical ages (between 0.25 and 0.50 days), but the SOA mass simulated by the
411   model is slightly lower than the measurements at the shortest photochemical ages (less
412   than 0.25 days) even when accounting for measurement uncertainties. In this
413   parameterization, most of the SOA produced comes from the P-S/IVOCs, and
414   uncertainties in the model with respect to these compounds likely explain the
415   overestimation observed at longer photochemical ages. As discussed in the introduction,
416   a major goal in this work is to better constrain the amount of SOA formed from the
417   oxidation of P-S/IVOCs, and the following two model cases (ROB + ZHAO + TSI and
418   WOR + ZHAO + TSI) seek to incorporate new measurements to better constrain the box
419   model with respect to the P-S/IVOCs.

420   When the yield, rate constants, and initial concentrations of P-IVOCs are
421   constrained using the field measurements reported in Zhao et al. (2014) (ROB + ZHAO +
422   TSI), the SOA mass simulated by the model shows much better agreement with the
423   measurements at longer photochemical ages (Fig. 3 et 4). There is a slight over-prediction
424   at 2 days of photochemical aging, but the model is still within the range of measurements
425   of very aged urban SOA reported by De Gouw and Jimenez (2009). The parameterization
426   reported in Robinson et al. (2007) for P-S/IVOCs is based on one study of the photo-
427   oxidation of diesel emissions from a generator (Robinson et al., 2007). The results
428   obtained here for the better constrained ROB + ZHAO + TSI case indicate that the initial
429   concentrations of P-IVOCs as well as the P-IVOC yields within ROB + TSI are too high
430   which leads to over-prediction of SOA concentration at longer photochemical ages. On
431   the other hand, the SOA mass simulated in ROB + ZHAO + TSI is biased low at shorter
432   photochemical ages (less than 1 day). Similar to other recent studies (Ortega et al., 2016;
433   Hayes et al., 2015; Gentner et al., 2012), there may be unexplained SOA precursors not
434   included in the model which rapidly form SOA or yields for fast-reacting species
435   including certain VOCs may be biased low. Both of these possibilities are explored in the
436   other model cases discussed below.

437   The WOR + ZHAO + TSI case simulates higher SOA concentrations at shorter
438   photochemical ages compared to the previous case (ROB + ZHAO + TSI), but it is still
439   biased low at shorter photochemical ages. The more rapid SOA formation is due to the

updated SVOC volatility distribution in this model case compared to the cases that use the Robinson et al. (2007) distribution. Specifically, as shown in Fig. 2F, there is a higher relative concentration of gas phase SVOCs in the $c^* = 10^2$ bin, and SOA formation from these precursors is relatively fast due to their low initial volatility leading to increased SOA formation during the first hours of photochemical aging. This case suggests that P-SVOCs in their highest volatility bin ($c^* = 10^2$ bin) that are emitted by motor vehicles may be responsible for some of the observed rapid SOA formation within the South Coast Air Basin. When observing the SOA mass simulated at photochemical ages higher than 1 day, the simulation is similar to ROB + ZHAO + TSI. There is better model/measurement agreement than for the ROB + TSI case, but a small over-prediction is observed in the comparison to the reactor data at 2 days of photochemical aging.

Also shown in the right-hand panels of Fig. 3 and 4 are the results with the updated yields for the VOCs that account for gas phase chamber wall losses. For these last three cases (ROB + MA, ROB + ZHAO + MA, and WOR + ZHAO + MA), the rate of SOA formation at short photochemical ages is faster because the secondary SVOC mass from the oxidation of the VOC precursors is distributed into lower volatility bins compared to the Tsimpidi et al. (2010) parameterization. In the ROB + MA case (Fig. 3D and 4D), similar to ROB + TSI, an over-prediction is obtained at longer photochemical ages. However, there is an improvement in the model at the shortest photochemical ages, but the simulated mass is still lower than the measurements even when considering the measurement uncertainty. Both of these cases perform less well for SOA formation within the South Coast Air Basin, and therefore the remainder of this study is focused on the other four model cases. In the cases with the updated yields, the SOA concentration reaches a plateau at longer photochemical ages, whereas in the model cases using the original yields from the TSI parameterization, the SOA mass concentration continues to increase due to aging. Overall, the model cases using the updated yields for V-SOA show improvement for the shorter photochemical ages, and the evolution of SOA concentration as a function of photochemical age better corresponds to the various measurements taken at Pasadena, aboard the NOAA P3, and from the OFR.

Finally, the WOR + ZHAO + MA case shows the best model/measurement agreement among the different cases used in this work. The SOA mass simulated at longer photochemical ages better agrees with measurements compared to the WOR + ZHAO + TSI case, and model/measurement agreement is obtained for the reactor and the airborne data at longer photochemical ages as shown in Fig. 4F. Also, the WOR + ZHAO + MA simulation is more consistent with the fit of the measurements (Fig. 3F) in which the SOA mass remains nearly constant at longer photochemical ages. In contrast, the WOR + ZHAO + TSI case does not follow this trend as the SOA mass keeps increasing between 2 and 3 days age, which is not observed in the measurements. As mentioned above, the model used for this work doesn't include fragmentation reactions, but this

479   option is unlikely to be the explanation for the over-prediction observed at > 2 days for
480   the WOR + ZHAO + TSI case. According to the OFR data from Ortega et al. (2016), the
481   mass of OA starts to decay due to fragmentation at approximately 10 days of
482   photochemical aging. In this work, the model is run only up to 3 days, which is much
483   shorter than the age when fragmentation appears to become important. Fig. 4F indicates
484   that including additional P-SVOC mass in the model and accounting for gas-phase wall
485   losses in chamber studies improves SOA mass concentration simulations with respect to
486   the measurements. However, in the WOR + ZHAO + MA case there is still a slight
487   under-prediction of SOA formed at shorter photochemical ages (between 0.05 and 0.5
488   days), and this discrepancy is observed in all the other model cases.

3.1.2 SOA concentration estimated at Pasadena: fossil and non-fossil fractions

491   In the top panel of Figure 5, the box model is compared against the urban SOA
492   determined by PMF analysis of the AMS measurements at Pasadena (Hayes et al., 2013).
493   In the bottom panel of the same figure the model is compared against the fossil and non-
494   fossil fraction of urban SOA as obtained from ^{14}C measurements reported in Zotter et al.
495   (2014). Both panels show measurements and predictions corresponding to 12:00 – 15:00
496   local time, when SOA concentrations peaked due to longer photochemical ages (5 hours
497   on average) as well as the arrival of emissions transported from source-rich western
498   regions of the South Coast Air Basin.

499   Similar to the results in Fig. 3 and 4 for short photochemical ages, the SOA mass
500   simulated by the ROB + ZHAO + TSI case is biased low in Fig. 5A. The ROB + ZHAO
501   + MA, WOR + ZHAO + TSI, and WOR + ZHAO + MA cases show better
502   model/measurement agreement as the simulated SOA mass is within the measurement
503   uncertainty or essentially equal to the lower limit of the concentration that is defined by
504   the measurement uncertainty. Fig. 5A also allows evaluation of the contribution of each
505   precursor type to the SOA at Pasadena. For the four cases displayed, the P-SVOCs and P-
506   IVOCs are responsible for 70 – 86 % of the urban SOA formation. Thus, more than half
507   of the urban SOA is attributed to these precursors even in the MA parameterizations
508   where the model is run with the updated yields, which doubles V-SOA compared to the
509   cases using the yields reported from Tsimpidi et al. (2010). Furthermore, 7 – 30 % of the
510   measured urban SOA is due to V-SOA where the range of values is due to the uncertainty
511   in the measurements as well as the difference in simulated V-SOA concentration for each
512   case.

513   According to the ^{14}C measurements, an average of 71 ± 3 % of urban SOA at
514   Pasadena is fossil carbon, which is thought to be due to the importance of vehicular
515   emissions, especially during the morning rush hour (Hayes et al., 2015; Zotter et al.,
516   2014; Bahreini et al., 2012). In general, the box model gives results consistent with the

517   ^{14}C measurements. To make this comparison, the simulated SOA is apportioned between
518   fossil S-SOA, fossil I-SOA, fossil V-SOA, cooking S-SOA, and biogenic V-SOA. The
519   last two apportionments correspond to non-fossil carbon. The apportionment of SOA into
520   these categories is possible because the box model calculates the SOA formed from each
521   precursors compound or lumped species individually. Then the SOA mass from a
522   precursor can be attributed to fossil or non-fossil depending on the identity of the
523   precursor following an approach similar to Hayes et al. (2015). Briefly, the fossil S-SOA
524   is formed from P-SVOCs emitted with hydrocarbon-like OA (HOA), which is a surrogate
525   for vehicular POA. Second, cooking S-SOA is formed from P-SVOCs emitted with
526   cooking-influenced OA (CIOA). The concentrations of HOA and CIOA were determined
527   previously using PMF analysis. Fossil V-SOA is formed from aromatics, alkanes, and
528   olefins while isoprene and terpenes are responsible for biogenic V-SOA. The treatment of
529   IVOCs in the comparison with the ^{14}C measurements has been updated from our 2015
530   study. Previously, it was assumed that P-IVOCs were co-emitted with cooking-influenced
531   OA, but the recent work of Zhao et al. (2014) indicates that petroleum sources contribute
532   substantially to IVOC emissions. Therefore, the IVOCs are considered entirely fossil
533   carbon in order to obtain the results shown in Fig. 5B.

534   As seen in Fig. 5B, for all the model cases, cooking S-SOA dominates the non-
535   fossil fraction and biogenic VOCs have only a small contribution to non-fossil urban
536   SOA. This result is consistent with our previous work, and indicates agreement between
537   the model and ^{14}C measurements cannot be achieved without including an urban source
538   of non-fossil carbon such as P-SVOCs from cooking. With respect to fossil SOA, more
539   S-SOA is formed when using the volatility distribution of vehicular POA reported from
540   Worton et al. (2014) due to the greater proportion of gas-phase of P-SVOCs. When the
541   V-SOA yields are updated in the model (MA parameterizations), there is a corresponding
542   increase in both fossil and non-fossil V-SOA.

543   When comparing the fossil/non-fossil carbon split, all the cases are either in
544   agreement with the measurement within its uncertainty, or slightly lower. Starting with
545   the ROB + ZHAO + TSI case, the fossil fraction increases from 73 % to 77 % in each
546   case as VOCs or P-SVOCs from vehicle emissions have greater importance for SOA
547   formation. While the uncertainties reported in Zotter et al. (2014) were 71 ± 3 %, there
548   are likely additional errors due to different factors that may influence the model or
549   measurements. For example, the SOA forming potential of cooking emissions remains
550   uncertain since no parameterization specific to this source has been published, to our
551   knowledge. Alternatively, a portion of the P-IVOCs may be from cooking sources rather
552   than entirely from fossil sources as is assumed above (Klein et al., 2016). Taking the
553   WOR + ZHAO + MA case as an example, since it is the best performing case in this
554   work, model/measurement agreement is obtained within measurement uncertainties if one
555   assumes that 15 – 38 % of P-IVOCs come from cooking emissions. Ultimately, the

556 differences observed in the comparison with the ^{14}C data are very likely smaller than
557 these errors discussed here, and it is concluded that all the model cases perform equally
558 well with respect to the fossil/non-fossil carbon split.

559   As reported in Gentner et al. (2012), emissions from petroleum derived fuels such
560 as diesel and gasoline have an important contribution to the formation of SOA. However,
561 there have been conflicting results regarding the relative contributions of diesel versus
562 gasoline emissions (Bahreini et al., 2012; Gentner et al., 2012). In this work, the relative
563 contribution of different SOA sources is estimated following a procedure similar to that
564 previously published in Hayes et al. (2015), and the results are shown in Fig. S2 of the
565 supporting information. Briefly, the source apportionment method follows four steps.
566 First, after classifying the SOA mass from isoprene and terpenes as biogenic V-SOA, the
567 remaining V-SOA is attributed to gasoline emissions since the diesel contribution to V-
568 SOA is small (~3 %) (Hayes et al., 2015). Second, for the diesel and gasoline
569 contribution to S-SOA, 70(±10) % of HOA is emitted from diesel vehicles with the
570 remainder from gasoline vehicles (Hayes et al., 2013), and thus it is assumed for the
571 source apportionment that 70% (30%) of vehicular P-SVOCs are from diesel (gasoline)
572 vehicles. Third, the S-SOA from cooking sources is calculated separately in the model,
573 where the initial concentration of cooking P-SVOCs is estimated using the measured
574 CIOA concentration and the method described in Section 2.2.2 above. Lastly, the
575 fractional contributions to I-SOA mass is difficult to determine since there are still
576 uncertainties about the sources of IVOCs. According to Zhao et al. (2014), petroleum
577 sources other than on-road vehicles likely contribute substantially to primary IVOCs, but
578 evidence exists that cooking may be a source of IVOCs as well (Klein et al., 2016). Thus,
579 while we attribute I-SOA to these two sources, we do not distinguish the sources. The
580 estimated source apportionment in Fig S2 attributes urban SOA as follows: 4% to
581 biogenic V-SOA, 21% to gasoline V-SOA, 9% to gasoline S-SOA, 22 % to diesel S-
582 SOA, and 28 % to cooking S-SOA. The remaining 26 % is I-SOA that is either due to
583 cooking or off-road emissions of P-IVOCs.

584   It should be noted that according to McDonald et al. (2015), the emissions from
585 vehicles have decreased over time (i.e. between 1970 and 2010) due to regulations in
586 California. Warneke et al. (2012) have observed also that the emission ratios of some
587 SOA precursors (i.e. ΔVOC/ΔCO) have remained constant between 2002 and 2010,
588 while absolute concentrations have decreased. On the other hand, cooking and off-road
589 emissions are subject to different regulations in California, and the ratios of cooking or
590 off-road emissions to vehicular emissions have likely changed with time, which means
591 that the source apportionment results for urban SOA presented here will be specific to
592 2010.

593

3.2 SOA formation versus precursor oxidation rate constant

It is important to evaluate the contribution of different classes of precursors to SOA formation, and the relative contributions of VOCs, P-SVOCs, and P-IVOCs have not been well-constrained by previous studies as discussed in the introduction. Recent results from Ortega et al. (2016) point to the importance of fast-reacting precursors for urban SOA during CalNex, and we can use their results to provide an additional constraint on our box model. The fraction of SOA formed from each precursor class as a function of the precursor rate constant is displayed in Figure 6. A large majority of the V-SOA mass has precursor rate constants ranging from approximately 3×10^{-12} to 1×10^{-10} cm^3 $molec^{-1}$ s^{-1} (log k_{OH} -11.5 to -10.0). Aromatic species including toluene, 1,3,5-TMB, and 1,2,4-TMB that produce significant V-SOA as shown in previous studies generally have rate constants in this range (Hayes et al., 2015; Dzepina et al., 2009). On the other hand, the I-SOA and S-SOA are formed from compounds that have on average higher rate constants with a narrower range of values of 1×10^{-11} to 1×10^{-10} cm^3 $molec^{-1}$ s^{-1} (log k_{OH} -11.0 to -10.0). It is important to note that the measurements of IVOCs used here allow the rate constants of these precursors to be taken from published work or estimated using structure-function relationships as described previously (Zhao et al., 2014). For S-SOA, the rate constant is the aging rate constant reported originally by Robinson et al. (2007).

The right-axis of Fig. 6 shows the correlation (R^2) of different VOCs with the maximum concentration of SOA formed using the OFR as a function of their oxidation rate constants as reported in Ortega et al. (2016). This analysis of the OFR data allows us to constrain the rate constants of the most important SOA precursors. A detailed description of how the R^2 values were obtained can be found in Ortega et al. (2016). According to the R^2 data, the VOC compounds that correlate best with maximum SOA formation potential are those that have log k_{OH} rate constants ranging from -10.5 to -10.0. Similarly, in all four model cases most of the SOA formed comes from species with log k_{OH} values in the range -11 to -10.

On the other hand, when comparing the percentage of SOA mass simulated by the model with the observed R^2 values, all of the four cases are not entirely consistent with the R^2 data. According to the model, more SOA mass is formed from precursors in the bin ranging from -11.0 to -10.5 (the majority of mass formed comes from P-IVOCs) rather than the bin ranging from -10.5 to -10.0. In contrast, the R^2 value is higher for the more reactive bin. It is important to remember that the rate constants used for the unspeciated P-IVOCs are estimated as their lower limits (Zhao et al., 2014). If the P-IVOCs were fully speciated and the actual rate constants were used in the model, then some of the I-SOA mass would likely move from the -11.0 to -10.5 bin into the -10.5 to -10.0 bin. If either fast-reacting precursors were missing in the model, or if the rate

632 constants of the currently-implemented precursors were too small, then correcting either
633 error would shift the relative distribution shown in Fig. 6 towards faster-reacting SOA
634 precursors. In turn, the trend in the percentage of modeled SOA mass may more closely
635 follow the trend in R^2 values. Lastly, the higher P-SVOC concentrations in the WOR +
636 ZHAO + TSI and WOR + ZHAO + MA cases (Fig. 6B and D) slightly improve the
637 comparison with the R^2 data since additional SOA mass is formed from precursors in the
638 -10.5 to -10.0 bin. These findings highlight again the important contribution of fast-
639 reacting compounds, including P-S/IVOCs, to SOA formation in the South Coast Air
640 Basin.

641 ## 3.3 Volatility distribution of OA

642   Based on the evaluations carried out up to this point on the six model cases, the
643 WOR + ZHAO + MA case seems to most closely reproduce the observations. The entire
644 volatility distribution of the OA, precursors, and secondary gas phase organics is
645 therefore analyzed for this model case. Figure 7 shows this distribution for three selected
646 photochemical ages: 0, 5, and 36 h. The figure allows us to track the evolution of SOA
647 and secondary gas phase organics from each precursor class in terms of their
648 concentration and volatility and also to evaluate the reduction of precursor
649 concentrations. For the model results, the volatility distribution of all organics resolved
650 by precursor class, except for the VOCs and P-IVOCs, can be taken directly from the
651 model. To determine the volatility distribution of the VOCs and P-IVOCs, the SIMPOL.1
652 method (Pankow and Asher, 2008) is used to estimate the effective saturation
653 concentration of each compound or lumped species in the model. Also included in Fig. 7,
654 in the bottom-right panel, is the observed volatility distribution for the Pasadena ground
655 site, which is an average of measurements collected during 12:00 – 15:00 local time and
656 corresponds to 5 h of photochemical aging. For the measurements, the volatility
657 distribution of VOCs was determined using GC-MS data (Borbon et al., 2013) whereas
658 the IVOC distribution is taken from Zhao et al. (2014). The volatility distribution of
659 SVOCs was determined using combined thermal denuder AMS measurements (see the
660 supporting information for further details).

661   For the volatility distribution of the model at time 0, the concentrations of P-
662 SVOCs and P-IVOCs monotonically increases with the value of c*. However, a
663 discontinuity in the mass concentration exists between the bins c* = 10^2 and 10^3 µg m^{-3}.
664 This discontinuity can be explained by several factors. First, the measured IVOCs mass
665 concentration in the c* = 10^3 bin is very low, and since the initial concentrations of
666 IVOCs in the model are constrained by the field measurements, the model will also have
667 very low concentrations. Zhao et al. (2014) have already noted that the concentration of
668 P-IVOCs in this bin is relatively low when compared to the volatility distribution from
669 Robinson et al. (2007). Another possible explanation is the presence of cooking sources,

670   which in the model are responsible for substantial P-SVOC mass (~50%) but may have a
671   smaller contribution to the P-IVOC mass.

672   During oxidation the volatility distribution evolves and the concentration of
673   secondary organics increases in the bins between $c* = 10^{-1}$ and 10^3 µg m^{-3} (inclusive), and
674   the largest portion of SOA is found in the $c* = 1$ µg m^{-3} bin. This result is due to the
675   partitioning of the organic mass to the particle phase and the lack of particle phase
676   reactions in the model, which leads to very slow oxidation rates for species found in the
677   lower volatility bins. After 36 h, a large portion of the precursors have been reacted,
678   although some primary and secondary material remains in the gas phase giving rise to
679   more gradual SOA formation.

680   In Fig. 7, it is possible to compare the measured volatility distribution with the
681   model simulation at 5 h of photochemical aging. It should be noted that the relatively
682   high concentrations of VOCs in the model compared to the measurements are due to the
683   model containing VOCs for which measurements were not obtained in Pasadena. There
684   are 47 VOCs used in the model and only 19 VOCs were measured. However, the
685   remaining VOCs have been measured in other urban locations (Borbon et al., 2013;
686   Warneke et al., 2007) and thus it is assumed they are also present in the South Coast Air
687   Basin. For this work, we include these 28 remaining VOCs by assuming that they are also
688   emitted in the South Coast Air Basin with identical emission ratios (ΔVOC/ΔCO). When
689   comparing only VOCs measured and modeled (shown in hollow black bars), the results
690   are consistent (3.1, 3.6 and 2.2 µg m^{-3} from bins $c* = 10^7$ to 10^9 versus 3.8, 3.7 and 2.2 µg
691   m^{-3} for the measurements). On the other hand, the model appears to have a low bias for
692   the concentrations of P-IVOCs (0.16, 0.63, 0.89 and 2.3 µg m^{-3} from bins $c* = 10^3$ to 10^6
693   versus 0.21, 1.39, 2.65 and 3.82 µg m^{-3} for the measurements). This low bias is seen for
694   each volatility bin and could possibly be explained by either oxidation rate constants that
695   are too high or ΔIVOC/ΔCO ratios that are too low. The latter explanation seems more
696   likely given that the rate constants estimated using surrogate compounds and structure-
697   activity relationships for the unspeciated P-IVOCs are generally lower limits (Zhao et al.,
698   2014), which would result in a high bias rather than a low bias. The ΔIVOC/ΔCO ratios
699   may be low because the photochemical age between 00:00 – 6:00 local time is not strictly
700   zero, and some oxidation may have occurred during the period used to determine the ratio
701   values. Emission ratios such as ΔIVOC/ΔCO facilitate incorporating P-IVOC emissions
702   into 3-D models that already use CO emissions inventories, and the ΔIVOC/ΔCO ratios
703   reported here could be used for this purpose. However, the resulting I-SOA
704   concentrations should be considered lower limits given that the emission ratios, and also
705   the rate constants, are likely themselves lower limits.

706   For the measurements of SVOCs, all the mass in bins lower than 10^{-2} µg m^{-3} are
707   lumped into this bin for Fig. 7 since the model does not contain lower volatility bins. In

708 addition, the 10^1 and 10^2 µg m^{-3} bins are not well-resolved because the thermal denuder
709 did not consistently reach temperatures low enough (less than 37°C) to resolve SVOCs in
710 this range of volatilities. Thus, the 10^1 µg m^{-3} bin may contain some higher volatility
711 particulate mass although this contribution is expected to be small due to the low particle
712 phase fraction of compounds in the 10^2 µg m^{-3} bin. With these considerations in mind, the
713 volatility distribution of the SVOCs is somewhat different in the model compared to the
714 measurements. Most notably, the model does not form a significant amount of lower
715 volatility SOA in the 10^{-2} µg m^{-3} bin, whereas the measurements have a much higher
716 concentrations in this bin. A factor that may explain this difference between the volatility
717 distributions is the lack of particle phase reactions that continue to transform SOA into
718 lower volatility products, a process which is not considered in the model. One example of
719 a particle phase reaction is the formation of SOA within deliquesced particles, including
720 the partitioning of glyoxal to the aqueous phase to produce oligomers as discussed in
721 Ervens and Volkamer (2010). However, when comparing the total amount of particle
722 phase SVOCs, it seems that the model reproduces reasonably well the measurements (6.7
723 versus 9.0 µg m^{-3}) as expected based on the comparisons of the total SOA concentration
724 discussed above. In addition, the total amount of SVOCs (particle and gas phase) are
725 similar (12.3 vs 11.8 µg m^{-3}), although it is difficult to determine from measurements the
726 gas phase concentration of SVOCs in the 10^2 µg m^{-3} bin due to the lack of particle mass
727 in this bin under ambient concentrations as well as the limited temperature range of the
728 thermal denuder system.

729 Recently, Woody et al. (2016) published a paper that modeled SOA over
730 California using the Environmental Protection Agency's Community Multiscale Air
731 Quality Model that had been updated to include a VBS treatment of SOA (CMAQ-VBS).
732 As discussed in that paper, the modeled P-S/IVOC emission inventories remain an
733 important source of uncertainty in 3-D grid-based models. In that previous study several
734 different ratios of P-S/IVOCs-to-POA emissions were evaluated against measurements,
735 and it was found that a ratio of 7.5 gave the best agreement between the CMAQ-VBS
736 model and observations. From the results shown in Fig. 7 at a photochemical age of 0 h, a
737 P-S/IVOC-to-POA ratio of 5.2 is calculated. This ratio is different from that determined
738 by Woody et al. (2016), and may be biased low due to possibly low ΔIVOC/ΔCO
739 emission ratios as discussed earlier in this section, but it serves as both a useful lower
740 bound and has the advantage of being determined from empirical measurements of
741 aerosols rather than by tuning a model to match measured SOA concentrations. As stated
742 in Woody et al. (2016), the higher ratio may compensate for other missing (or
743 underrepresented) formation pathways in SOA models.

744

4. CONCLUSION

We have used several data sets from recently published papers to better constrain and evaluate urban SOA formation pathways and precursors, especially P-SVOCs and P-IVOCs, within a custom-built box model. The use of the box model facilitates the incorporation of these new data sets as well as the evaluation of a number of model cases. When measurements of IVOCs are used to constrain the concentrations of P-IVOCs, such as in the ROB + ZHAO + TSI and ROB + ZHAO + MA cases, a large improvement of the model at longer photochemical age is observed. However, these model cases are still biased low at shorter photochemical ages. By constraining the P-SVOCs additionally with measurements of those precursors, such as in the WOR + ZHAO + TSI case, better model/measurement agreement is obtained at shorter photochemical ages, yet the model is still biased low. The WOR + ZHAO + MA case, which incorporates state-of-the-art measurements of P-SVOCs and P-IVOCs and also accounts for the effect of chamber wall-losses on VOC yields, best simulates SOA formation, although some low bias at short photochemical ages remains. This bias may be due to low $\Delta IVOC/\Delta CO$ emissions ratios or IVOC oxidation rate constants for which the estimated values are too low. It is also possible that additional sources or SOA formation pathways are missing from the model. Moreover, a P-S/IVOC-to-POA ratio of 5.2 is determined, which can be combined with POA emission inventories to constrain the emissions of P-S/IVOCs in gridded chemical transport models. All the model cases are able to correctly simulate the fossil/non-fossil carbon split at the Pasadena ground site providing support for the performance of the model.

In addition to evaluating the model performance with respect to SOA concentration, the rates of SOA formation are compared against measurements as well. This aspect of the study was enhanced by the use of OFR data to constrain SOA formation potential for up to 3 days of photochemical aging (at 1.5×10^{6} molec OH cm^{-3}). The model cases that include multi-generation oxidative aging predict substantial SOA increases after 1.5 days of aging, which is not consistent with the OFR measurements. In contrast, model cases in which aging is omitted and instead SOA yields for VOCs are corrected for gas phase wall-losses in chamber experiments predict little change in the SOA concentration after 1.5 days. These results highlight the uncertainties associated with aging schemes for SOA from VOCs, which are often implemented in SOA models. Implementing instead corrected yields for VOCs results in similar amounts of SOA but formation rates versus time that are more consistent with observations.

In all six of the model cases, a large majority of the urban SOA at Pasadena is the result of P-SVOC and P-IVOC oxidation. While this result alone cannot be taken as conclusive due to the uncertainties in the model parameters, further evidence for the importance of P-SVOCs and P-IVOCs is obtained by analyzing the percentage of SOA

783   formed at long photochemical ages (~1.5 days) as a function of the precursor rate
784   constant. Highly reactive VOCs (e.g. decane, xylenes, and trimethylbenzenes) have been
785   previously found to strongly correlate with SOA formation potential, and P-IVOCs and
786   P-SVOCs have rate constants similar to these highly reactive VOCs (log k_{OH} = -11.0 to
787   -10.0). In contrast, the rate constants for the VOCs that are the largest contributors to
788   SOA are generally smaller (log k_{OH} -11.5 to -10.5), which further suggests that VOCs are
789   less important urban SOA precursors unless there are some highly reactive VOCs that are
790   not included in the model that produce a substantial amount of SOA.

791   Lastly, the modeled volatility distribution of the total (gas and particle phase)
792   organic mass between $C^* = 10^{-2}$ and 10^{10} ug m^{-3} is analyzed at three ages and compared
793   against volatility-resolved measurements. While the total concentrations of gas and
794   particle phase SVOCs are reasonably well simulated, at the same time there are important
795   differences between the measured and modeled volatility distribution of SVOCs. These
796   differences highlight the need for further studies of the chemical pathways that may give
797   rise to SOA in low volatility bins at $C^* = 10^{-2}$ ug m^{-3} and lower.

798

ACKNOWLEDGEMENTS

800   This work was partially supported by a Natural Science and Engineering Research
801   Council of Canada (NSERC) Discovery Grant (RGPIN/05002-2014), le Fonds de
802   recherche - Nature et technologies (FRQNT) du Québec (2016-PR-192364), and the
803   Université de Montréal. AMO and JLJ were supported by CARB 11-305 and EPA STAR
804   83587701-0. This manuscript has not been reviewed by EPA and thus no endorsement
805   should be inferred. We gratefully acknowledge VOC data provided by J. de Gouw and
806   J.B. Gilman.

807

REFERENCES

809   Ahmadov, R. McKeen, S. A. Robinson, A. L. Bahreini, R. Middlebrook, A. M. de Gouw,
810   J. A. Meagher, J. Hsie, E. Y. Edgerton, E. Shaw, S. and Trainer, M.: A volatility
811   basis set model for summertime secondary organic aerosols over the eastern
812   United States in 2006, J. Geophys. Res.-Atmos., 117, D06301, 2012
813   Atkinson, R. and Arey, J.: Atmospheric degradation of volatile organic compounds,
814   Chem. Rev., 103, 4605-4638, 2003
815   Bahreini, R. Middlebrook, A. M. de Gouw, J. A. Warneke, C. Trainer, M. Brock, C. A.
816   Stark, H. Brown, S. S. Dube, W. P. Gilman, J. B. Hall, K. Holloway, J. S. Kuster,
817   W. C. Perring, A. E. Prevot, A. S. H. Schwarz, J. P. Spackman, J. R. Szidat, S.
818   Wagner, N. L. Weber, R. J. Zotter, P. and Parrish, D. D.: Gasoline emissions

819   dominate over diesel in formation of secondary organic aerosol mass, Geophys.
820   Res. Lett., 39, L06805, 2012
821 Borbon, A. Gilman, J. B. Kuster, W. C. Grand, N. Chevaillier, S. Colomb, A.
822   Dolgorouky, C. Gros, V. Lopez, M. Sarda-Esteve, R. Holloway, J. Stutz, J.
823   Petetin, H. McKeen, S. Beekmann, M. Warneke, C. Parrish, D. D. and de Gouw,
824   J. A.: Emission ratios of anthropogenic volatile organic compounds in northern
825   mid-latitude megacities: Observations versus emission inventories in Los Angeles
826   and Paris, J. Geophys. Res.-Atmos., 118, 2041-2057, 2013
827 Carter, W. P. L.: Development of the SAPRC-07 chemical mechanism, Atmos. Environ.,
828   44, 5324-5335, 2010
829 Chan, A. W. H. Kautzman, K. E. Chhabra, P. S. Surratt, J. D. Chan, M. N. Crounse, J. D.
830   Kuerten, A. Wennberg, P. O. Flagan, R. C. and Seinfeld, J. H.: Secondary organic
831   aerosol formation from photooxidation of naphthalene and alkylnaphthalenes:
832   implications for oxidation of intermediate volatility organic compounds (IVOCs),
833   Atmos. Chem. Phys., 9, 3049-3060, 2009
834 Christensen, J. H. Krishna Kumar, K. Aldrian, E. An, S.-I. Cavalcanti, I. F. A. de Castro,
835   M. Dong, W. Goswami, A. Hall, A. Kanyanga, J. K. Kitoh, A. Kossin, J. Lau, N.-
836   C. Renwick, J. Stephenson, D. B. Xie, S.-P. and Zhou, T.: Climate Change 2013:
837   The Physical Scientific Basis. Contribution of Working Group I to the Fifth
838   Assessment Report of the Intergovernmental Panel on Climate Change. 2013
839 De Gouw, J. and Jimenez, J. L.: Organic Aerosols in the Earth's Atmosphere, Environ.
840   Sci. Technol., 43, 7614-7618, 2009
841 DeCarlo, P. F. Ulbrich, I. M. Crounse, J. de Foy, B. Dunlea, E. J. Aiken, A. C. Knapp, D.
842   Weinheimer, A. J. Campos, T. Wennberg, P. O. and Jimenez, J. L.: Investigation
843   of the sources and processing of organic aerosol over the Central Mexican Plateau
844   from aircraft measurements during MILAGRO, Atmos. Chem. Phys., 10, 5257-
845   5280, 2010
846 Dockery, D. W. and Pope, C. A.: Acute respiratory effects of particulate air-pollution,
847   Annu. Rev. Publ. Health, 15, 107-132, 1994
848 Donahue, N. M. Chuang, W. Epstein, S. A. Kroll, J. H. Worsnop, D. R. Robinson, A. L.
849   Adams, P. J. and Pandis, S. N.: Why do organic aerosols exist? Understanding
850   aerosol lifetimes using the two-dimensional volatility basis set, Envir. Chem., 10,
851   151-157, 2013
852 Donahue, N. M. Robinson, A. L. Stanier, C. O. and Pandis, S. N.: Coupled partitioning,
853   dilution, and chemical aging of semivolatile organics, Environ. Sci. Technol., 40,
854   2635-2643, 2006
855 Dzepina, K. Cappa, C. D. Volkamer, R. M. Madronich, S. DeCarlo, P. F. Zaveri, R. A.
856   and Jimenez, J. L.: Modeling the Multiday Evolution and Aging of Secondary
857   Organic Aerosol During MILAGRO 2006, Environ. Sci. Technol., 45, 3496-3503,
858   2011
859 Dzepina, K. Volkamer, R. M. Madronich, S. Tulet, P. Ulbrich, I. M. Zhang, Q. Cappa, C.
860   D. Ziemann, P. J. and Jimenez, J. L.: Evaluation of recently-proposed secondary
861   organic aerosol models for a case study in Mexico City, Atmos. Chem. Phys., 9,
862   5681-5709, 2009

863   Ervens, B. and Volkamer, R.: Glyoxal processing by aerosol multiphase chemistry:
864   towards a kinetic modeling framework of secondary organic aerosol formation in
865   aqueous particles, Atmos. Chem. Phys., 10, 8219-8244, 2010
866   Fountoukis, C. Megaritis, A. G. Skyllakou, K. Charalampidis, P. E. Denier van der Gon,
867   H. A. C. Crippa, M. Prévôt, A. S. H. Fachinger, F. Wiedensohler, A. Pilinis, C.
868   and Pandis, S. N.: Simulating the formation of carbonaceous aerosol in a
869   European Megacity (Paris) during the MEGAPOLI summer and winter
870   campaigns, Atmos. Chem. Phys., 16, 3727-3741, 2016
871   Gentner, Drew R. Isaacman, Gabriel Worton, David R. Chan, Arthur W. H. Dallmann,
872   Timothy R. Davis, Laura Liu, Shang Day, Douglas A. Russell, Lynn M. Wilson,
873   Kevin R. Weber, Robin Guha, Abhinav Harley, Robert A. and Goldstein, Allen
874   H.: Elucidating secondary organic aerosol from diesel and gasoline vehicles
875   through detailed characterization of organic carbon emissions, Proc. Natl. Acad.
876   Sci. USA, 109, 18318-18323, 2012
877   Hallquist, M. Wenger, J. C. Baltensperger, U. Rudich, Y. Simpson, D. Claeys, M.
878   Dommen, J. Donahue, N. M. George, C. Goldstein, A. H. Hamilton, J. F.
879   Herrmann, H. Hoffmann, T. Iinuma, Y. Jang, M. Jenkin, M. E. Jimenez, J. L.
880   Kiendler-Scharr, A. Maenhaut, W. McFiggans, G. Mentel, Th F. Monod, A.
881   Prevot, A. S. H. Seinfeld, J. H. Surratt, J. D. Szmigielski, R. and Wildt, J.: The
882   formation, properties and impact of secondary organic aerosol: current and
883   emerging issues, Atmos. Chem. Phys., 9, 5155-5236, 2009
884   Hayes, P. L. Carlton, A. G. Baker, K. R. Ahmadov, R. Washenfelder, R. A. Alvarez, S.
885   Rappenglück, B. Gilman, J. B. Kuster, W. C. de Gouw, J. A. Zotter, P. Prévôt, A.
886   S. H. Szidat, S. Kleindienst, T. E. Offenberg, J. H. Ma, P. K. and Jimenez, J. L.:
887   Modeling the formation and aging of secondary organic aerosols in Los Angeles
888   during CalNex 2010, Atmos. Chem. Phys., 15, 5773-5801, 2015
889   Hayes, P. L. Ortega, A. M. Cubison, M. J. Froyd, K. D. Zhao, Y. Cliff, S. S. Hu, W. W.
890   Toohey, D. W. Flynn, J. H. Lefer, B. L. Grossberg, N. Alvarez, S. Rappenglueck,
891   B. Taylor, J. W. Allan, J. D. Holloway, J. S. Gilman, J. B. Kuster, W. C. De
892   Gouw, J. A. Massoli, P. Zhang, X. Liu, J. Weber, R. J. Corrigan, A. L. Russell, L.
893   M. Isaacman, G. Worton, D. R. Kreisberg, N. M. Goldstein, A. H. Thalman, R.
894   Waxman, E. M. Volkamer, R. Lin, Y. H. Surratt, J. D. Kleindienst, T. E.
895   Offenberg, J. H. Dusanter, S. Griffith, S. Stevens, P. S. Brioude, J. Angevine, W.
896   M. and Jimenez, J. L.: Organic aerosol composition and sources in Pasadena,
897   California, during the 2010 CalNex campaign, J. Geophys. Res.-Atmos., 118,
898   9233-9257, 2013
899   Heald, C. L. Coe, H. Jimenez, J. L. Weber, R. J. Bahreini, R. Middlebrook, A. M.
900   Russell, L. M. Jolleys, M. Fu, T. M. Allan, J. D. Bower, K. N. Capes, G. Crosier,
901   J. Morgan, W. T. Robinson, N. H. Williams, P. I. Cubison, M. J. DeCarlo, P. F.
902   and Dunlea, E. J.: Exploring the vertical profile of atmospheric organic aerosol:
903   comparing 17 aircraft field campaigns with a global model, Atmos. Chem. Phys.,
904   11, 12673-12696, 2011
905   Hodzic, A. and Jimenez, J. L.: Modeling anthropogenically controlled secondary organic
906   aerosols in a megacity: a simplified framework for global and climate models,
907   Geosci. Model Dev., 4, 901-917, 2011

908 Jimenez, J. L. Canagaratna, M. R. Donahue, N. M. Prevot, A. S. H. Zhang, Q. Kroll, J. H.
909   DeCarlo, P. F. Allan, J. D. Coe, H. Ng, N. L. Aiken, A. C. Docherty, K. S.
910   Ulbrich, I. M. Grieshop, A. P. Robinson, A. L. Duplissy, J. Smith, J. D. Wilson,
911   K. R. Lanz, V. A. Hueglin, C. Sun, Y. L. Tian, J. Laaksonen, A. Raatikainen, T.
912   Rautiainen, J. Vaattovaara, P. Ehn, M. Kulmala, M. Tomlinson, J. M. Collins, D.
913   R. Cubison, M. J. Dunlea, E. J. Huffman, J. A. Onasch, T. B. Alfarra, M. R.
914   Williams, P. I. Bower, K. Kondo, Y. Schneider, J. Drewnick, F. Borrmann, S.
915   Weimer, S. Demerjian, K. Salcedo, D. Cottrell, L. Griffin, R. Takami, A.
916   Miyoshi, T. Hatakeyama, S. Shimono, A. Sun, J. Y. Zhang, Y. M. Dzepina, K.
917   Kimmel, J. R. Sueper, D. Jayne, J. T. Herndon, S. C. Trimborn, A. M. Williams,
918   L. R. Wood, E. C. Middlebrook, A. M. Kolb, C. E. Baltensperger, U. and
919   Worsnop, D. R.: Evolution of Organic Aerosols in the Atmosphere, Science, 326,
920   1525-1529, 2009
921 Klein, F. Platt, S. M. Farren, N. J. Detournay, A. Bruns, E. A. Bozzetti, C. Daellenbach,
922   K. R. Kilic, D. Kumar, N. K. Pieber, S. M. Slowik, J. G. Temime-Roussel, B.
923   Marchand, N. Hamilton, J. F. Baltensperger, U. Prevot, A. S. H. and El Haddad,
924   I.: Characterization of Gas-Phase Organics Using Proton Transfer Reaction Time-
925   of-Flight Mass Spectrometry: Cooking Emissions, Environ. Sci. Technol., 50,
926   1243-1250, 2016
927 Krechmer, J. E. Pagonis, D. Ziemann, P. J. and Jimenez, J. L.: Quantification of Gas-
928   Wall Partitioning in Teflon Environmental Chambers Using Rapid Bursts of Low-
929   Volatility Oxidized Species Generated in Situ, Environ. Sci. Technol., 50, 5757-
930   5765, 2016
931 Kroll, J. H. Ng, N. L. Murphy, S. M. Flagan, R. C. and Seinfeld, J. H.: Secondary organic
932   aerosol formation from isoprene photooxidation, Environ. Sci. Technol., 40,
933   1869-1877, 2006
934 Matsunaga, A. and Ziemann, P. J.: Gas-Wall Partitioning of Organic Compounds in a
935   Teflon Film Chamber and Potential Effects on Reaction Product and Aerosol
936   Yield Measurements, Aerosol Sci. Technol., 44, 881-892, 2010
937 McDonald, B. C. Goldstein, A. H. and Harley, R. A.: Long-Term Trends in California
938   Mobile Source Emissions and Ambient Concentrations of Black Carbon and
939   Organic Aerosol, Environ. Sci. Technol., 49, 5178-5188, 2015
940 Ng, N. L. Kroll, J. H. Chan, A. W. H. Chhabra, P. S. Flagan, R. C. and Seinfeld, J. H.:
941   Secondary organic aerosol formation from m-xylene, toluene, and benzene,
942   Atmos. Chem. Phys., 7, 3909-3922, 2007
943 Odum, J. R. Hoffmann, T. Bowman, F. Collins, D. Flagan, R. C. and Seinfeld, J. H.:
944   Gas/particle partitioning and secondary organic aerosol yields, Environ. Sci.
945   Technol., 30, 2580-2585, 1996
946 Ortega, A. M. Hayes, P. L. Peng, Z. Palm, B. B. Hu, W. Day, D. A. Li, R. Cubison, M. J.
947   Brune, W. H. Graus, M. Warneke, C. Gilman, J. B. Kuster, W. C. de Gouw, J.
948   Gutiérrez-Montes, C. and Jimenez, J. L.: Real-time measurements of secondary
949   organic aerosol formation and aging from ambient air in an oxidation flow reactor
950   in the Los Angeles area, Atmos. Chem. Phys., 16, 7411-7433, 2016
951 Pankow, J. F.: An absorption model of the gas aerosol partitionning incolved in the
952   formation of secondary organic aerosol, Atmos. Environ., 28, 189-193, 1994

953   Pankow, J. F. and Asher, W. E.: SIMPOL.1: a simple group contribution method for
954   predicting vapor pressures and enthalpies of vaporization of multifunctional
955   organic compounds, Atmos. Chem. Phys., 8, 2773-2796, 2008
956   Presto, A. A. Miracolo, M. A. Donahue, N. M. and Robinson, A. L.: Secondary Organic
957   Aerosol Formation from High-NOx Photo-Oxidation of Low Volatility
958   Precursors: n-Alkanes, Environ. Sci. Technol., 44, 2029-2034, 2010
959   Robinson, A. L. Donahue, N. M. Shrivastava, M. K. Weitkamp, E. A. Sage, A. M.
960   Grieshop, A. P. Lane, T. E. Pierce, J. R. and Pandis, S. N.: Rethinking organic
961   aerosols: Semivolatile emissions and photochemical aging, Science, 315, 1259-
962   1262, 2007
963   Ryerson, T. B. Andrews, A. E. Angevine, W. M. Bates, T. S. Brock, C. A. Cairns, B.
964   Cohen, R. C. Cooper, O. R. de Gouw, J. A. Fehsenfeld, F. C. Ferrare, R. A.
965   Fischer, M. L. Flagan, R. C. Goldstein, A. H. Hair, J. W. Hardesty, R. M.
966   Hostetler, C. A. Jimenez, J. L. Langford, A. O. McCauley, E. McKeen, S. A.
967   Molina, L. T. Nenes, A. Oltmans, S. J. Parrish, D. D. Pederson, J. R. Pierce, R. B.
968   Prather, K. Quinn, P. K. Seinfeld, J. H. Senff, C. J. Sorooshian, A. Stutz, J.
969   Surratt, J. D. Trainer, M. Volkamer, R. Williams, E. J. and Wofsy, S. C.: The
970   2010 California Research at the Nexus of Air Quality and Climate Change
971   (CalNex) field study, J. Geophys. Res.-Atmos., 118, 5830-5866, 2013
972   Spracklen, D. V. Jimenez, J. L. Carslaw, K. S. Worsnop, D. R. Evans, M. J. Mann, G. W.
973   Zhang, Q. Canagaratna, M. R. Allan, J. Coe, H. McFiggans, G. Rap, A. and
974   Forster, P.: Aerosol mass spectrometer constraint on the global secondary organic
975   aerosol budget, Atmos. Chem. Phys., 11, 12109-12136, 2011
976   Tsimpidi, A. P. Karydis, V. A. Zavala, M. Lei, W. Molina, L. Ulbrich, I. M. Jimenez, J.
977   L. and Pandis, S. N.: Evaluation of the volatility basis-set approach for the
978   simulation of organic aerosol formation in the Mexico City metropolitan area,
979   Atmos. Chem. Phys., 10, 525-546, 2010
980   Volkamer, R. Jimenez, J. L. San Martini, F. Dzepina, K. Zhang, Q. Salcedo, D. Molina,
981   L. T. Worsnop, D. R. and Molina, M. J.: Secondary organic aerosol formation
982   from anthropogenic air pollution: Rapid and higher than expected, Geophys. Res.
983   Lett., 33, 2006
984   Warneke, C. de Gouw, J. A. Holloway, J. S. Peischl, J. Ryerson, T. B. Atlas, E. Blake, D.
985   Trainer, M. and Parrish, D. D.: Multiyear trends in volatile organic compounds in
986   Los Angeles, California: Five decades of decreasing emissions, J. Geophys. Res.-
987   Atmos., 117, 2012
988   Warneke, C. McKeen, S. A. de Gouw, J. A. Goldan, P. D. Kuster, W. C. Holloway, J. S.
989   Williams, E. J. Lerner, B. M. Parrish, D. D. Trainer, M. Fehsenfeld, F. C. Kato, S.
990   Atlas, E. L. Baker, A. and Blake, D. R.: Determination of urban volatile organic
991   compound emission ratios and comparison with an emissions database, J.
992   Geophys. Res.-Atmos., 112, D10s47, 2007
993   Watson, J. G.: Visibility: Science and regulation, J. Air Waste Manag. Assoc., 52, 628-
994   713, 2002
995   Woody, M. C. Baker, K. R. Hayes, P. L. Jimenez, J. L. Koo, B. and Pye, H. O. T.:
996   Understanding sources of organic aerosol during CalNex-2010 using the CMAQ-
997   VBS, Atmos. Chem. Phys., 16, 4081-4100, 2016

998   Worton, D. R. Isaacman, G. Gentner, D. R. Dallmann, T. R. Chan, A. W. H. Ruehl, C.
999   Kirchstetter, T. W. Wilson, K. R. Harley, R. A. and Goldstein, A. H.: Lubricating
1000   Oil Dominates Primary Organic Aerosol Emissions from Motor Vehicles,
1001   Environ. Sci. Technol., 48, 3698-3706, 2014
1002   Ye, P. Ding, X. Hakala, J. Hofbauer, V. Robinson, E. S. and Donahue, N. M.: Vapor wall
1003   loss of semi-volatile organic compounds in a Teflon chamber, Aerosol Sci.
1004   Technol., 50, 822-834, 2016
1005   Zhang, Q. Jimenez, J. L. Canagaratna, M. R. Allan, J. D. Coe, H. Ulbrich, I. Alfarra, M.
1006   R. Takami, A. Middlebrook, A. M. Sun, Y. L. Dzepina, K. Dunlea, E. Docherty,
1007   K. DeCarlo, P. F. Salcedo, D. Onasch, T. Jayne, J. T. Miyoshi, T. Shimono, A.
1008   Hatakeyama, S. Takegawa, N. Kondo, Y. Schneider, J. Drewnick, F. Borrmann,
1009   S. Weimer, S. Demerjian, K. Williams, P. Bower, K. Bahreini, R. Cottrell, L.
1010   Griffin, R. J. Rautiainen, J. Sun, J. Y. Zhang, Y. M. and Worsnop, D. R.: Ubiquity
1011   and dominance of oxygenated species in organic aerosols in anthropogenically-
1012   influenced Northern Hemisphere midlatitudes, Geophys. Res. Lett., 34, 2007
1013   Zhang, X. Cappa, C. D. Jathar, S. H. McVay, R. C. Ensberg, J. J. Kleeman, M.l J. and
1014   Seinfeld, J. H.: Influence of vapor wall loss in laboratory chambers on yields of
1015   secondary organic aerosol, Proc. Natl. Acad. Sci. USA, 111, 5802-5807, 2014
1016   Zhao, Y. Hennigan, C. J. May, A. A. Tkacik, D. S. de Gouw, J. A. Gilman, J. B. Kuster,
1017   W. C. Borbon, A. and Robinson, A. L.: Intermediate-Volatility Organic
1018   Compounds: A Large Source of Secondary Organic Aerosol, Environ. Sci.
1019   Technol., 48, 13743-13750, 2014
1020   Zotter, P. El-Haddad, I. Zhang, Y. M. Hayes, P. L. Zhang, X. Lin, Y.-H. Wacker, L.
1021   Schnelle-Kreis, J. Abbaszade, G. Zimmermann, R. Surratt, J. D. Weber, R. J.
1022   Jimenez, J. L. Szidat, S. Baltensperger, U. and Prevot, A. S. H.: Diurnal cycle of
1023   fossil and nonfossil carbon using radiocarbon analyses during CalNex, J.
1024   Geophys. Res.-Atmos., 119, 6818-6835, 2014

1025

Table 1 Summary of the model cases used in this paper.

Case	Notes	References
1) ROB + TSI	P-S/IVOCs: Robinson et al. parameterization, and all SOA treated within VBS framework VOCs: Tsimpidi et al. parameterization with aging	Hayes et al. (2015) Robinson et al. (2007) Tsimpidi et al. (2010)
2) ROB + ZHAO + TSI	P-SVOCs: Robinson et al. parameterization, and all SOA treated within VBS framework P-IVOCs: Zhao et al. parameterization with aging VOCs: Tsimpidi et al. parameterization with aging	Robinson et al. (2007) Zhao et al. (2014) Tsimpidi et al. (2010)
3) WOR + ZHAO + TSI	P-SVOCs: Worton et al. volatility distribution for vehicular P-SVOCs, Robinson et al. volatility distribution for cooking P-SVOCs P-IVOCs: Zhao et al. parameterization with aging VOCs: Tsimpidi et al. parameterizations with aging	Robinson et al. (2007) Worton et al. (2014) Zhao et al. (2014) Tsimpidi et al. (2010)
4) ROB + MA	P-S/IVOCs: Robinson et al. parameterization, and all SOA treated within VBS framework VOCs: Updated VOCs yields, no aging of VOC oxidation products	Robinson et al. (2007) This work
5) ROB + ZHAO + MA	P-SVOCs: Robinson et al. parameterization, and all SOA treated within VBS framework P-IVOCs: Zhao et al. IVOC parameterization with aging VOCs: Updated VOCs yields, no aging of VOC oxidation products	Robinson et al. (2007) Zhao et al. (2014) This work
6) WOR + ZHAO + MA	P-SVOCs: Worton et al. volatility distribution for vehicular P-SVOCs, Robinson et al. volatility distribution for cooking P-SVOCs P-IVOCs: Zhao et al. IVOC parameterization with aging VOCs: Updated VOCs yields, no aging of VOC oxidation products	Robinson et al. (2007) Worton et al. (2014) Zhao et al. (2014) This work

Figure 1 Schematic of the chemical pathways leading to the formation of SOA in the box model where α is the SOA yield, k_{OH} is the rate constant of a species oxidized by OH radicals, and X_p is the particle-phase fraction of a species.
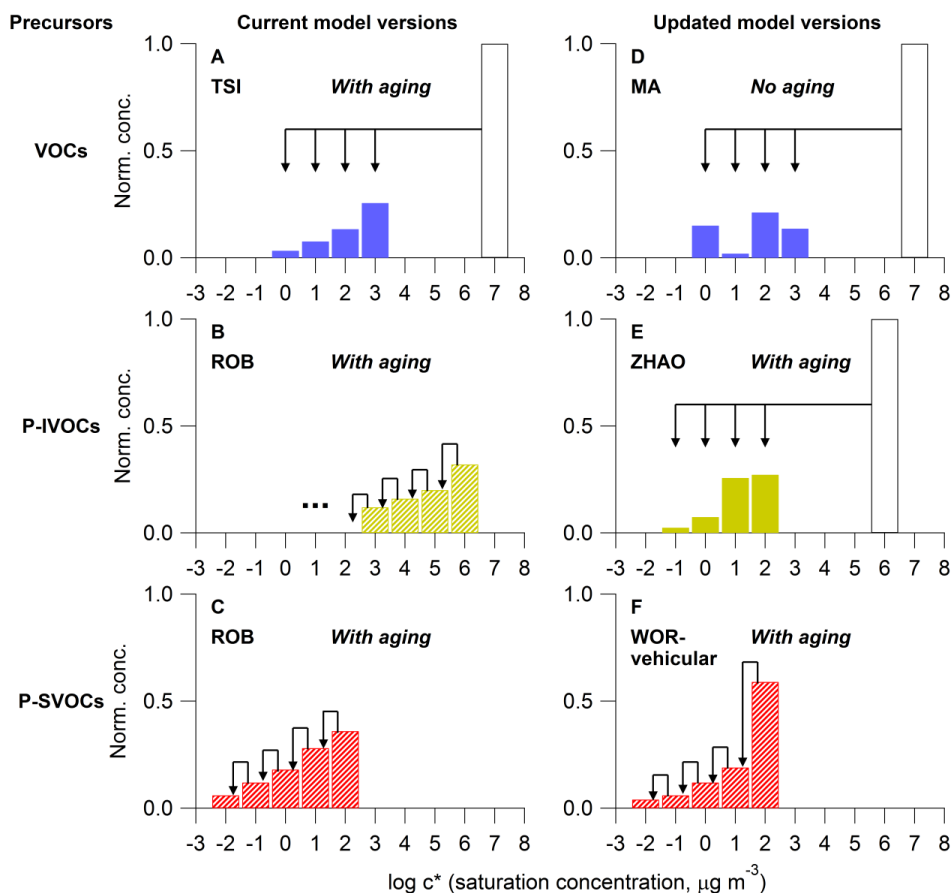
Figure 2 Schematic of the SOA formation parameterizations used in the model. The products formed are shown in different colors for each precursor. Note that the striped color bars indicate that the bins contain both primary and secondary organics. In panel **(A)** the parameterization of Tsimpidi et al. (2010) distributes the products of VOCs oxidation into four volatility bins. Panels **(B)** and **(C),** show the parameterization of Robinson et al. (2007) in which the volatility of the SOA precursors, specifically IVOCs and SVOCs, decrease by one order of magnitude per oxidation reaction. For P-IVOCs, aging continues to transfer mass to lower volatility bins (log c* < 2). Panel **(D)** shows the updated parameterization for VOC oxidation that accounts for gas phase wall losses, and Panel **(E)** shows the updated parameterization for P-IVOC oxidation that uses the speciated measurements of IVOCs from Zhao et al. (2014). In Panel **(F),** for the parameterization based on the measurements of Worton et al. (2014), the Robinson et al. (2007) volatility distribution is still used for the P-SVOCs emitted from cooking sources. Arrows representing the aging of SOA are omitted for clarity.
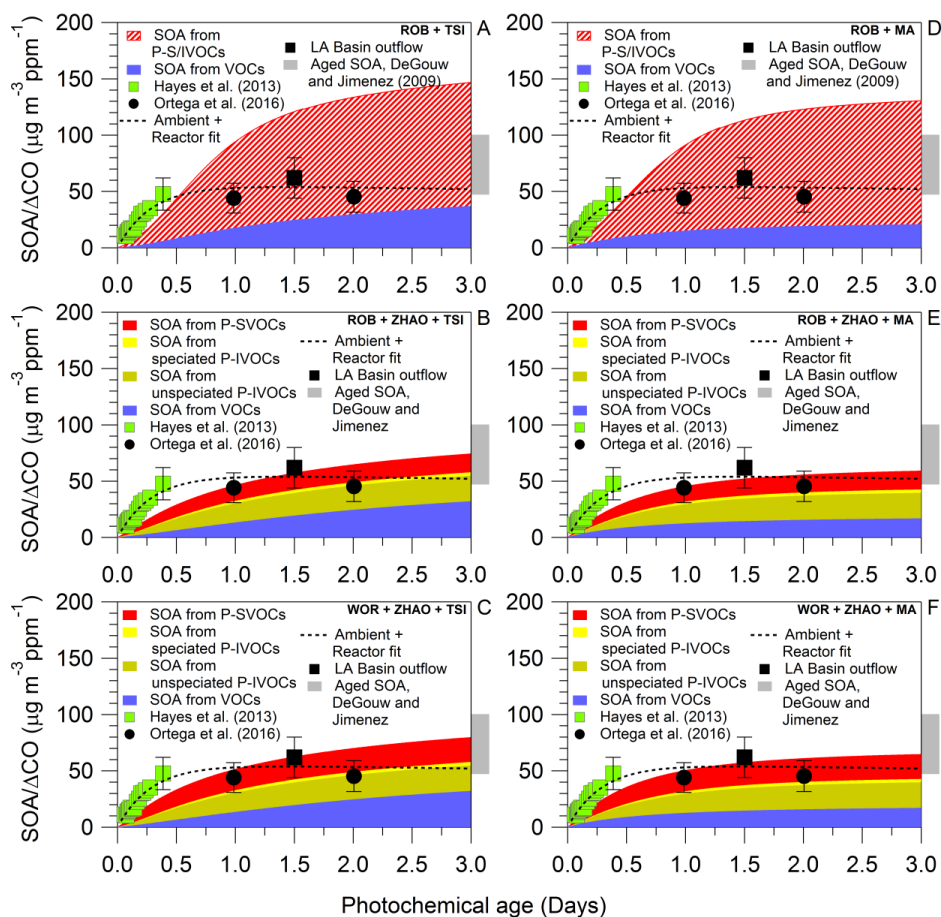
Figure 3 Predicted urban SOA mass by all six cases for up to 3 days of photochemical aging using a reference OH radical concentration of 1.5×10^6 molec cm^{-3}. Background SOA is not included in the figure. The SOA concentrations have been normalized to the background subtracted CO (ΔCO) concentration to account for changes in emission strengths and dilution. The SOA/ΔCO data determined from the ambient and OFR measurements at Pasadena as reported by Hayes et al. 2013 (green squares) and Ortega et al. 2016 (black circles) are shown. Also shown is SOA/ΔCO determined from measurements performed aboard the NOAA P3 research aircraft (black square) and reported by de Gouw and Jimenez (2009) (gray bar) for highly aged urban air masses. The fit for ambient and reactor data reported by Ortega et al. 2016 is also shown (dotted black line).
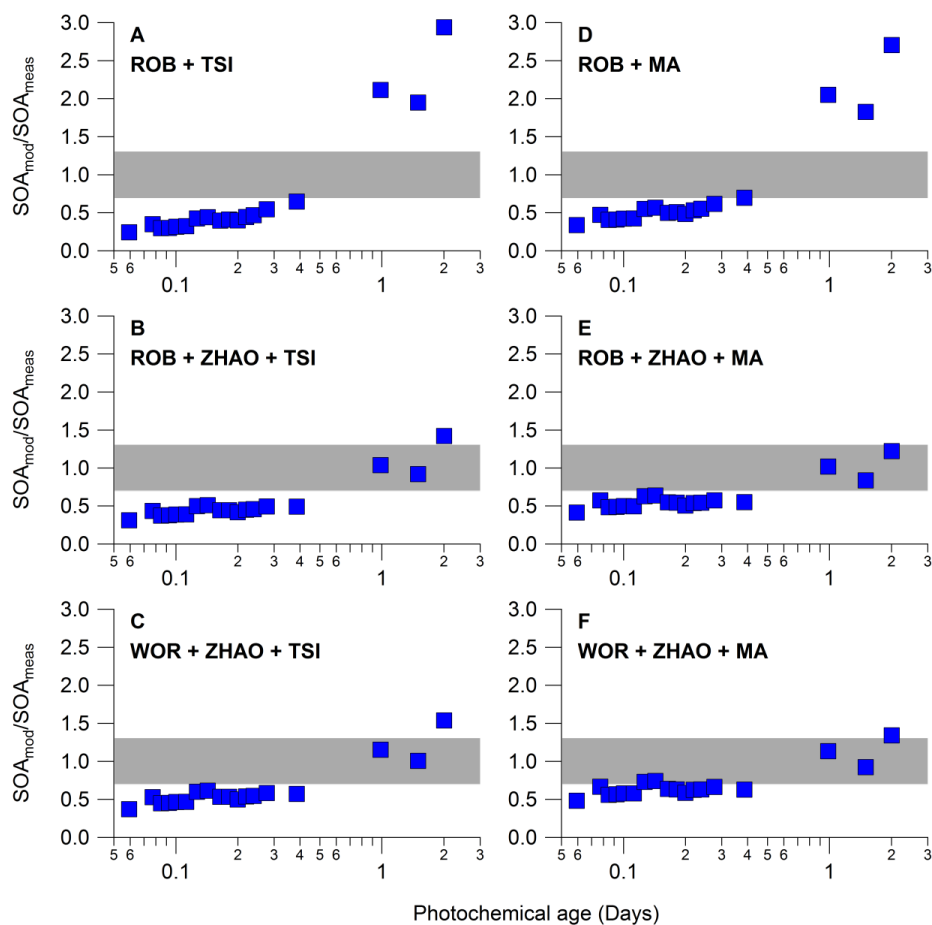
Figure 4 The ratio of the modeled-to-measured SOA concentrations (blue squares) for all model cases. The measurements are the same as used in Figure 1. The gray bar indicates ratios that would correspond to model results that are within the estimated ± 30 % uncertainty of the measurements.
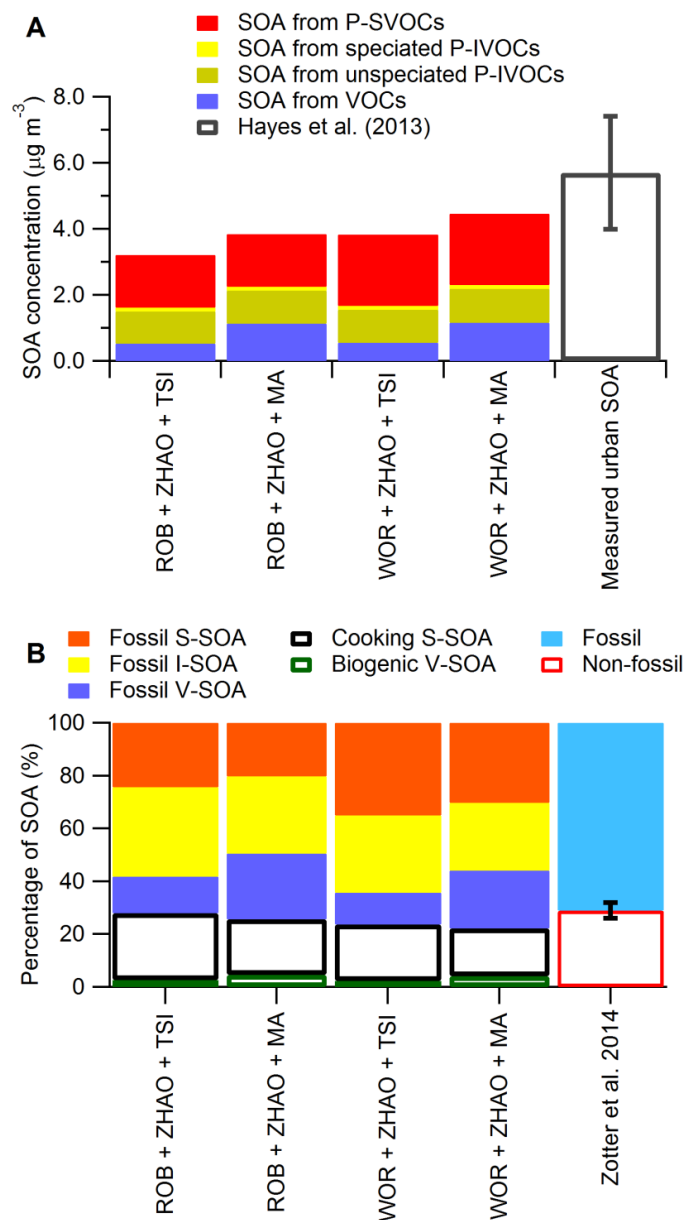
Figure 5 (A) Predicted and measured urban SOA mass for 12:00 – 15:00 local time at the Pasadena ground site. **(B)** The fractional mass of fossil S-SOA, fossil I-SOA, and fossil V-SOA, as well as cooking S-SOA and biogenic V-SOA for the same time and location. The percentage of urban SOA from fossil and non-fossil sources as reported in Zotter et al. (2014) is also displayed. The fossil sources are shown as solid bars and the non-fossil sources as hollow bars.
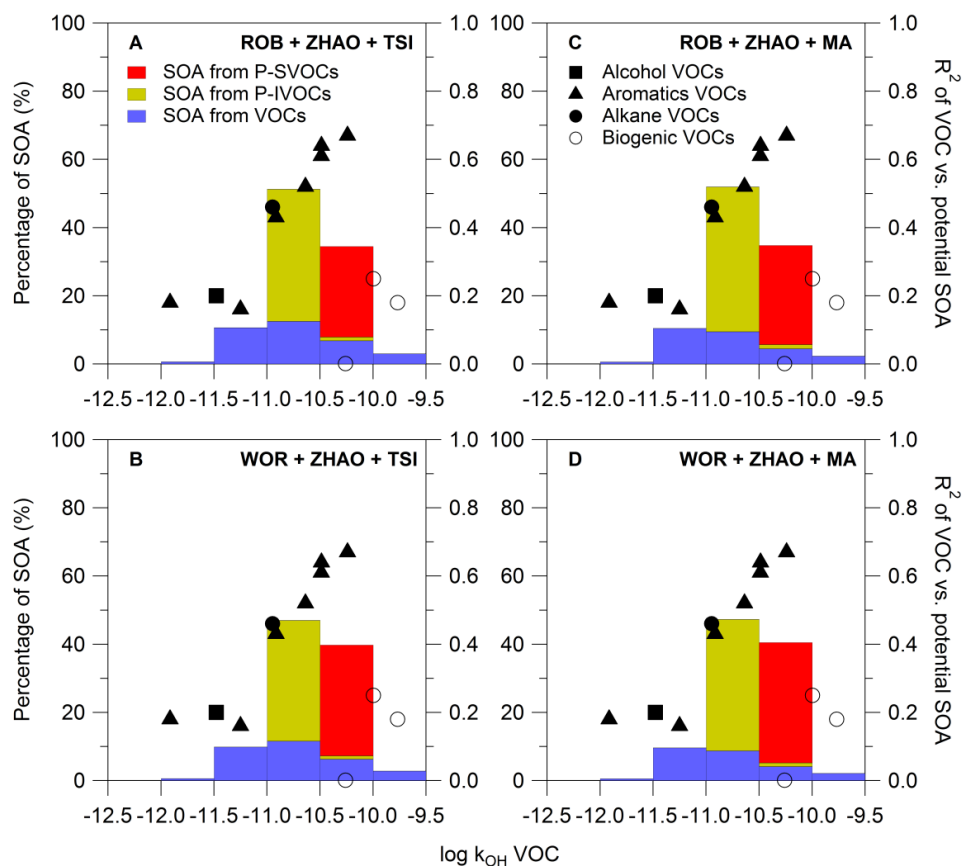
Figure 6 Percentage of SOA mass formed from different precursors at 1.5 days of photochemical aging (at 1.5×10^6 molec OH cm^{-3}) binned according to precursor rate constant. The correlations (R^2) between the concentrations of different VOCs and the maximum SOA concentration formed in the OFR as reported by Ortega et al. (2016) are represented by the markers. The shape of the marker indicates the chemical family to which each compound belongs. For the VOCs and the P-IVOCs the rate constant is the constant for the initial oxidation reaction.
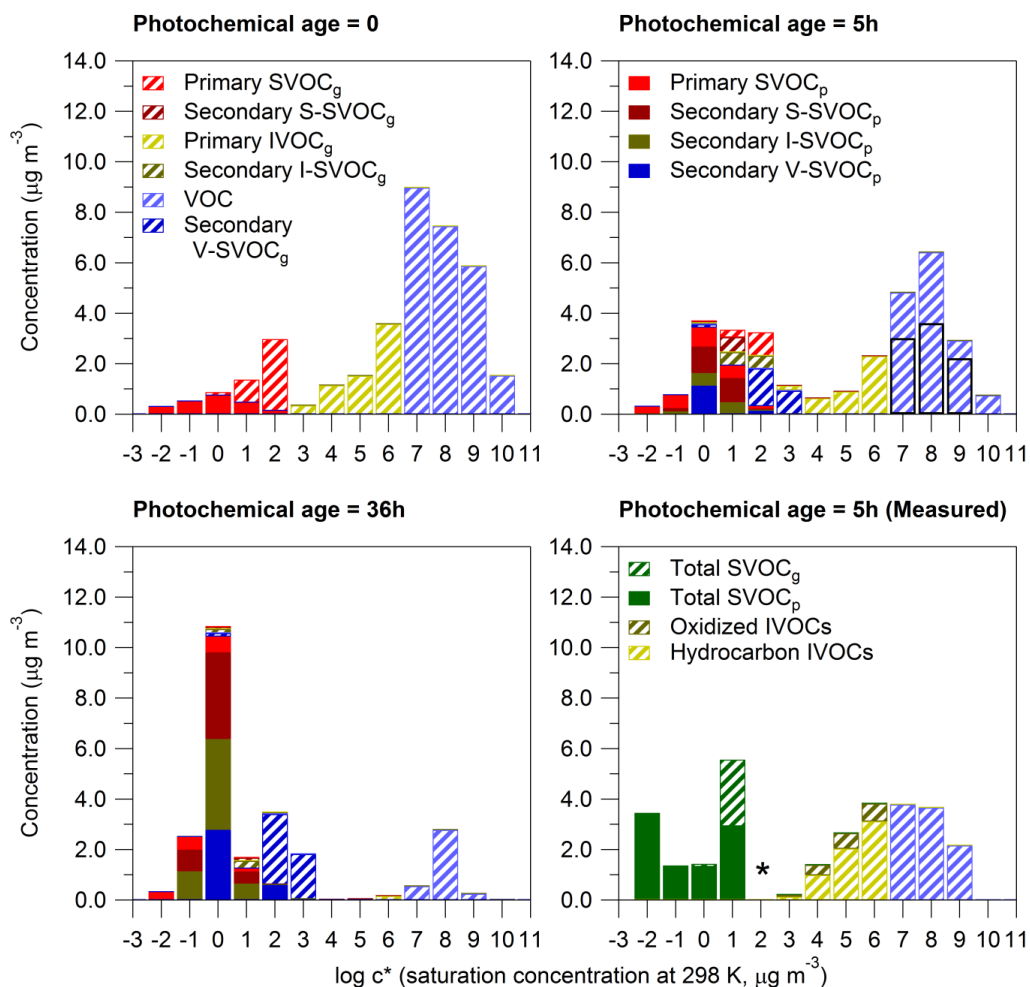
Figure 7 OA volatility distribution as simulated by the WOR + ZHAO + MA case displayed at different photochemical ages (0, 5, and 36 h). The partitioning of the species is indicated using patterned bars for gas phase and solid bars for particle phase mass. The bottom-right graph also shows the measured volatility distribution of OA. The SVOC volatility distribution is determined using a combined thermal denuder AMS system as described in the supporting information. The IVOC volatility distribution was previously published in Zhao et al. (2014), and the VOC distribution was determined from GC-MS measurements using the SIMPOL.1 model to estimate the volatility of each VOC. The asterisk in the bin log c* = 2 indicates that measurements are not available for this bin. It should be noted that not all the VOCs in the model were measured at Pasadena (see text for details). For direct visual comparison with the measurements, the simulated concentrations of only the VOCs measured at Pasadena are indicated by the black hollow bars in the bins log c* = 7, 8, and 9 μg m^{-3}.